

**WIND TUNNEL INVESTIGATION ON SURFACE-PRESSURES AND VORTEX FLOWOVER
DELTA WING AT HIGH ANGLES OF ATTACK AND FREE-STREAM VELOCITIES**

Salaheldin H. Omar

*Professor of Aerospace and Autonomous Systems Engineering and former Chair;
Talent and Technology Creativity Unit,
University of Tabuk, Saudi Arabia.
salaheldin.omar@outlook.com*

Abstract

Vortex flow is an important phenomenon associated with high agility aircrafts at super maneuvering rates, slender body of revolutions, highly swept back and delta wings, dynamical meteorology, physical oceanography and enhanced fuel/air mixing process inside the internal combustion chambers. This paper covers wind tunnel measurements of the steady surface-pressures over a carbon-fiber sharp-edged delta wing of aspect ratio 1 and sweep back angle of 76.0° at different speeds and angles of attack. Numerical calculations on the structure deformation of this wing test model have been performed using NASTRAN/PATRAN software packages. The predicted results have been correlated to the development of the vortex flow over the investigated delta wing.

Keywords: Vortex Flow, Vortex Breakdown, Vortex Dynamics, Delta Wing, Super Maneuvering Aircraft, High Agility Aircraft, Slender Body of Revolution, Wind Tunnel, Pressure Measurements, Delta Wing Structure Deformation, Modal Analysis, Data Acquisition Systems.

Nomenclatures

Cr - Wing root chord
 Re - Reynolds number based on chord length of the wing
 Λ - Aspect ratio
 r - Radius of viscous sub core
 λ - wave length
 ρ - Fluid density
 ρ_0 - Reference density (a pure constant)
 k - Number of waves
 δ - Local vortices thickness (vertical extent of mixing zone)
 $\Delta \rho$ - Density difference of two adjacent fluid streams
 ΔU - Difference between flow Velocities of two adjacent fluid streams
 ω - Angular velocity
 R - Radial distance from the centre of the vortex core
 $g' = g (\rho_2 - \rho_1)$ is the reduced gravity
 S - Local wing span
 U_∞ - Free stream speed
 x - Local chord-wise distance from wing apex
 y - Local span-wise distance from wing root "from wing line of

symmetry”
 Z - Local distance above wing surface
 h - Maximum wing profile thickness
 α - Wing angle of attack
 α_c - Vortex-core angle of attack
 Λ_c - Vortex-core sweep angle
 β - Wing angle side slip
 Λ_{LE} - Wing sweep back angle
 V_{swirl} - Vortex swirl velocity
 V_{axial} - Vortex axial velocity
 ϕ - Swirl angle = $\tan^{-1}(V_{swirl} / V_{axial})$
 C_p - Surface pressure coefficient

I. INTRODUCTION

1.1. The Vortex flow over delta wings

Vortex flow is an important phenomenon associated with high agility aircrafts at super maneuvering, rates, slender body of revolutions, highly swept back wings and delta wing, dynamical meteorology covering Thunderstorms, Sea breeze, Tornado, Hurricane, Mountain waves, and physical oceanography including oceanic waves, vortices, currents, long oceanic waves, atmospheric convection, and natural oscillations in air-sea interactions. High agility aircrafts maneuvering at high angles of attack might be affected by Asymmetrical and antisymmetrical vortex flow and breakdown leading to large side forces and yawing moments beyond the maximum moments affordable by the control surfaces.

1.2. Vortices over delta wings

In a homogeneous fluid, mixing requires enough energy necessary to overcome mechanical frictions, but in a stratified fluid additional energy is necessary to raise heavy fluid parcels and lower light fluid parcels against buoyancy forces increasing the potential energy and therefore the mixing can proceed spontaneously if the reduction in the kinetic-energy exceeds the increase in the potential-energy. Mixing of fluid parcels can be performed only if the initial density-difference is small enough to avoid an insurmountable gravitational barrier [1, 2] Thorpe, S. A. (1968, 1971), or if the initial velocity-shear is large enough to provide the necessary energy for the fluid mixing process to take place. The ratio between potential and kinetic energies has been defined as Richardson number “ Ri ”, with the numerator is the potential-energy barrier that mixing process must overcome to be performed and the denominator is the available kinetic energy of the shear flow.

Richardson number = $(g/\rho_0) \Delta\rho \delta / \Delta U^2$

[3] Richardson Lewis Fry (1922)

Kelvin-Helmholtz instability was first studied by Taylor in 1915 (Taylor, G. I., (1931) [4]) concluding that Richardson number must be less than $1/4$ for instability to occur, otherwise, the mixing process occurs only locally in a vicinity of the initial interface and will not therefore be able to spread over the whole system. The splitted flow streamlines of both sides of delta wing join each other at the separation line along the wing leading edge forming separated free shear layer of two

separated adjacent streams of different velocities, namely the lower velocity stream from the pressure side, and the higher velocity stream from the leeward side of the wing. The difference in the velocities of the two parallel streams of the separated shear layer initiate inviscid instability of a constant-vorticity layer in the interfacial region inside the free shear layer and generate laminar small waves which distort the boundaries of the region containing the vortices as in figure 1(a). The perturbations induce vertical velocities which force the perturbations and waves to grow into discrete vortices and therefore increasing the thickness of the free shear layer by moving away from the leading edge, figure 1 (b). Mixing layers are growing initiating big spiral vortices due to the known Kelvin-Helmholtz type instability. Each vorticity tends to entrain the other neighbored vorticity under the influence of their induced velocity forcing both vortices to rotate around one another in pair due to the nonlinear interaction. Every vorticity rotate slower at its outer part than close to the center initiating tails as shown in figure 1-C which merge into spirals during the pairing Piercy N. A. V. (1923) [5], Winant, C. et al (1974) [6]. The interfacial region of constant vorticity becomes periodically fatter and thinner, figure 1 (c) and the pairing process starts. The pairing process amplifies the spatial and irregularities in the vortex structure and increasing the variations in the length and strength of the vortex cores which are continually rotating around one another in pairs forming the rotating vortex lumps in the interfacial region of the free shear layer figure 1(d) and figure 2. The free shear layer rolls up into a vortex core by the impact of the vorticity induced flow velocities on both sides of vortex lumps within the free shear layer as shown in figure 1- (d and e), 2, and figure 3 of wind tunnel smoke and laser light sheet flow visualization over sharp edged delta wing after Omar Salaheldin H. Part III [7]. The primary vortex can be divided, after Earnshaw P. (1962) [8], into three regions, namely; the free shear layer, the rotational core, and viscous subcore as shown in figure 2. The free shear layer generated at the leading edge rolled up forming the primary vortex induces the outer flow of the primary vortex to reattach on the leeward side of the delta wing and is continually providing the boundary layer after the reattachment line with fresh air of high energy as illustrated in figure 2. The reattached flow moves from the reattachment line outboard toward the leading edge until it separates at the secondary separation line somewhere between the axis of the primary vortex and the leading edge in dependence of the flow condition "laminar/turbulent" forming the secondary vortex. Tertiary vortex may be initiated underneath the secondary vortex with a rotation in the same sense of the primary vortex.

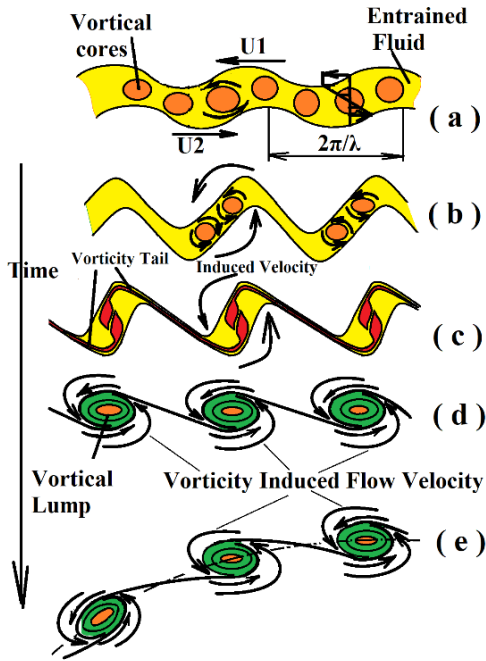


Figure 1 (a-e): Vortex pairing and lumps

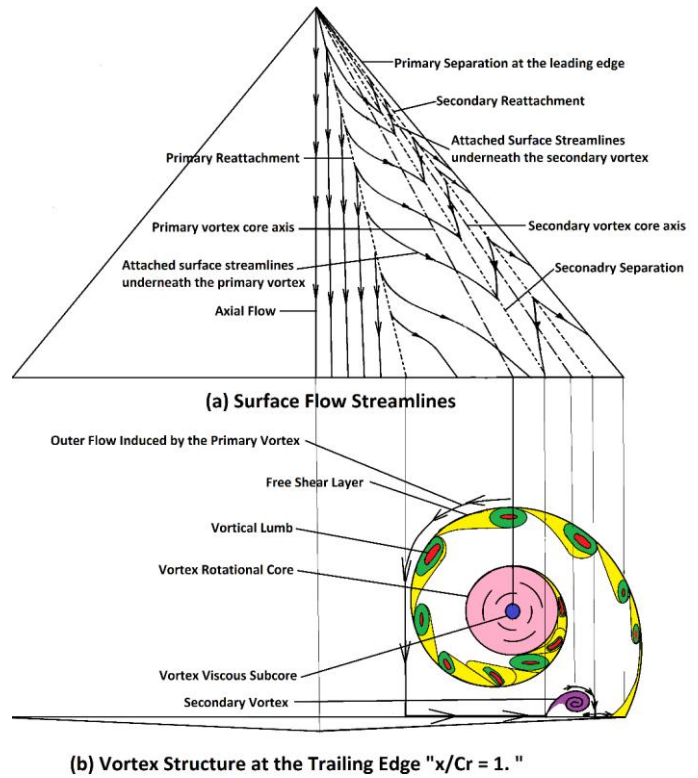


Figure 2: surface flow stream lines and vortex flow of a delta wing

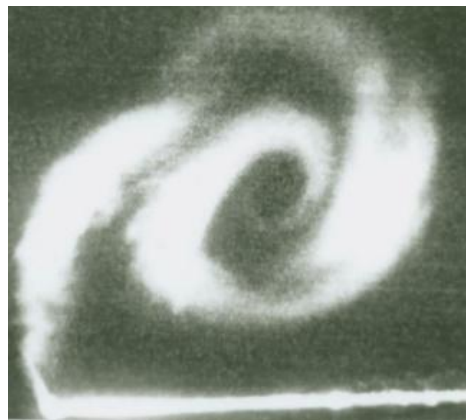


Figure 3: Laser smoke and light sheet illumination of the cross flow on a sharp edged delta wing, part III of this investigation Omar, Salaheldin H. et al [7]

1.4 Vortex Breakdown

Vortex breakdown is defined by Sarpkaya T. (1971) [9] as sudden sharp deformation of the vortex core structure resulting in expanding asymmetric flow around the vortex axis. Leibovich S. (1978) [10] and Garg A. & Leibovich S. (1979) [11] described vortex breakdown as a disturbance which decelerates the internal flow along the vortex axis up to a stagnation condition followed by reversing the flow direction. Vortex breakdown occurs, after Schade H., Michalke, A. (1962) [12] in dependence of the external pressure gradient and the degree of the divergence as indication of the vorticity convection along the vortex axis, and after Hall M. (1972) [13], it occurs in dependence of the magnitude of the flow swirling, as an indication of the vorticity shedded in the rolled up free shear layer, the external pressure gradient and the degree of the divergence, as indication of the vorticity convection along the vortex axis Schade H., Michalke, A. (1962) [12]. At a certain angle of attack the increased rate of generation of the vortices shedded in the vortex sheet exceeds the convection of these vortices leading to an increase in the concentrated vortices, which have limits on their maximum amount of vortices per unit area "critical vortices concentration". By exceeding these limits, the shedded vortices in the rolled up free shear layer cannot be compensated by the convection of the vortices, which is dependent on the increased component of the axial flow velocity by increasing the angle of attack, and gradually, the axial momentum becomes too weak to overcome the adverse pressure gradient, leading to a drastic increase in the interactions among the vortex-outer-core spirals, and to the formation of a stagnation point along the viscous subcore, subsequently, the vortex cannot maintain its organized structure leading to a spiral form or bubble form vortex breakdown, as in figure 4, spreading the vortices over a wider region and the excessive vortices are redistributed in the region aft the vortex-breakdown location reducing the vorticity concentration inside the vortex sheet. More details are available in Omar, Salaheldin H. (2020) [14].

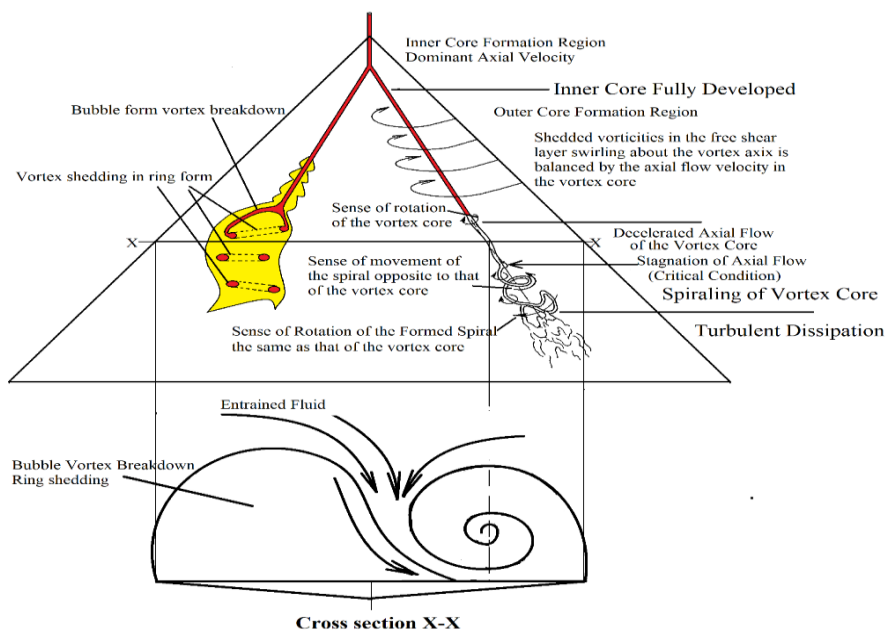


Figure 4: Vortex formation and breakdown over delta wings

II. EXPERIMENTAL SETUP

2.1. Wind tunnel facility and test condition

All experiments were carried out in low speed closed loop water cooled wind tunnel of TU Munich, Germany. The test section of the wind tunnel is open flow test section of 1.2 meter diameter, 72 m/s maximum speed, and 0.2-0.3 % turbulence shown in figure 5 (a, b, c, and d).

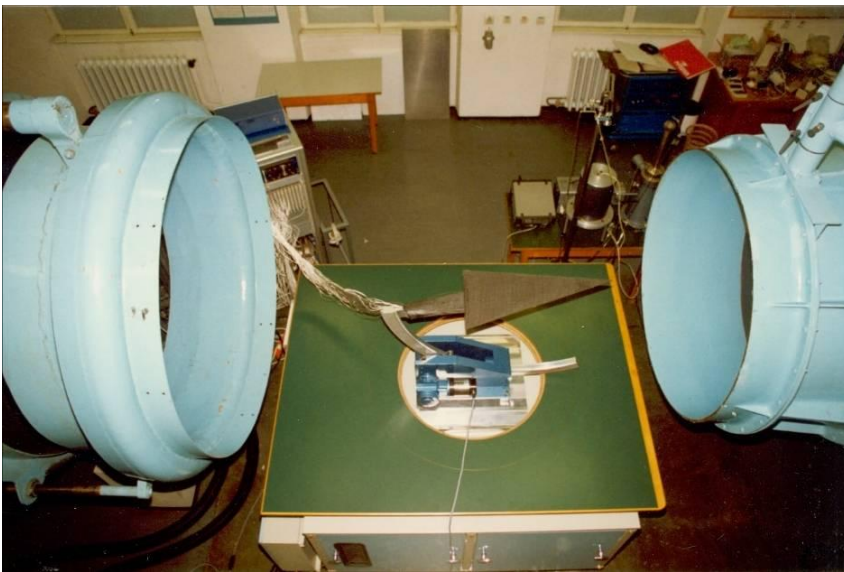


Fig. 5-a



Fig. 5-b

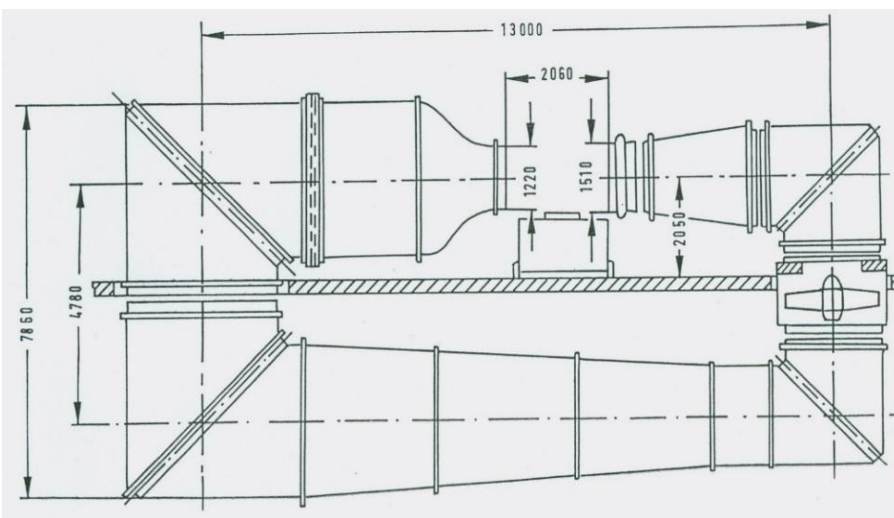


Fig. 5-c

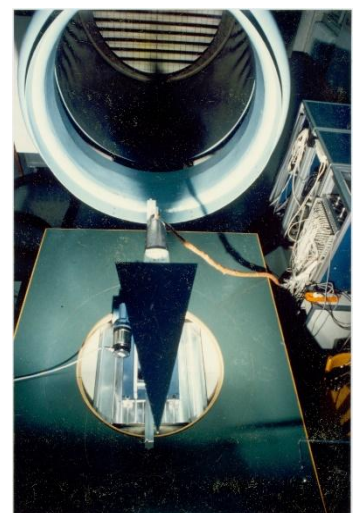


Fig. 5-d

Figure 5: Wind Tunnel Facility

2.2. Wind Tunnel Test Model

The wind tunnel test model is a sharp edged delta wing manufactured from carbon fibers to predict solely the aerodynamic forces by minimizing elastic forces and inertia forces, which interact mutually with the aerodynamic forces changing their predicted values. The development and breakdown of the vortex over the leeside of the delta wing as well as the vortex shedding at very high angles of attack up to 65° have been predicted.

The test model is a light weight, stiff, sharp edged delta wing made from carbon fibers of aspect ratio $\Lambda = 1$, sweep back angle Λ_{LE} of 76° , length of 670mm, chord of 335mm and maximum thickness h of 57mm as shown in figure 6 (a). A total number of 70 Kulite piezo resistive full differential miniature pressure transducers of the type CQ-107-093-5D as shown in figure 6 (b) are integrated in the leeside surface of the sharp edged delta wing using bent support "transducer-support configuration" if enough space inside the test model is available as shown in figure 7 (b). For locations of tightly spaces inside the test model, straight support "transducer-support-tube configuration" are used as shown in figure 7 (a). The transducers are integrated in the leeside surface of the delta wing along its right semi span at 5 sections located at $x/Cr=0.3$ "9 sensors", $x/Cr = 0.5$ "10 sensors", $x/Cr = 0.7$ "13 sensors", $x/Cr=0.8$ "13 sensors", and $x/Cr=0.9$ "25 sensors along its whole span as in figure 6 (a). All reference tubes of the pressure transducers are connected to the atmosphere of the wind tunnel room outside the wind tunnel test section through a common silicon tube and a cylinder for pressure-fluctuations damping, as shown in figure 8 to avoid the effect of any possible dynamic pressure inside the wing. The transformation functions of all 70 integrated transducer-support and transducer support-tube configurations have been predicted. The data acquisition system used in this investigation consists of 128 differential channels having amplifiers, anti-aliasing filters, sample and hold, multiplexer, 14 bit analog/digital converter of maximum sampling rate of 128 kHz. This system is connected to a PC for the control and to store the acquired signals, and connected to the supercomputer of LRZ Munich for the digital signal processing of the data as shown in figure 9. Steady and unsteady pressure measurements have been accomplished for zero sweep angle, at the following angle of attacks; 0, 2.5, 5, 7.5, 10, 12.5, 15, 17.5, 20, 25, 30, 35, 40, 45, 50, 55, 60, 65 degree, and at two free stream speed of 24m/s and 48m/s, in this paper only the static measurements at zero sideslip angle are presented. Measurements at different angles of sideslip as well as the unsteady measurements are under publications.

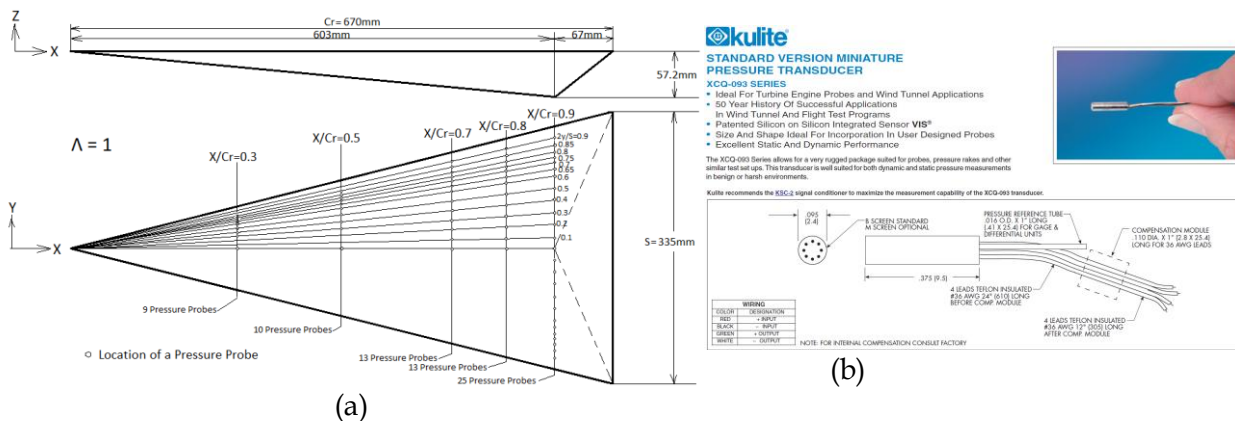


Figure 6 (a) Delta wing dimension and layout of the sensors, (b) Kulite pressure transducer

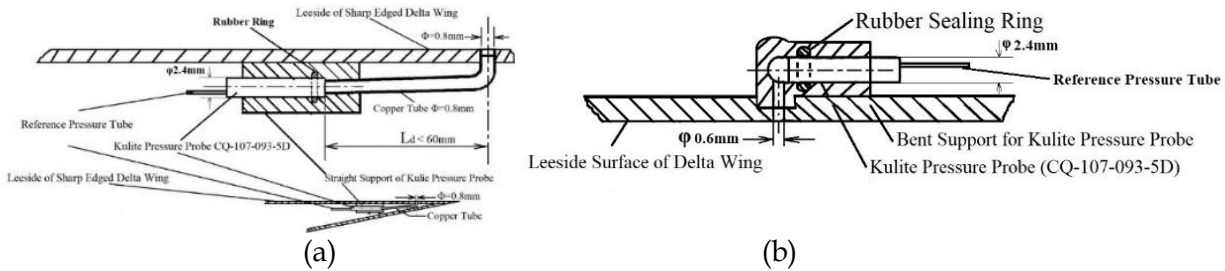


Figure 7: (a) Indirect integration of the straight support “transducer-support-tube configuration”, (b) Direct integration of the bent support “transducer-support configuration”.



Figure 8: The delta wing in the wind tunnel

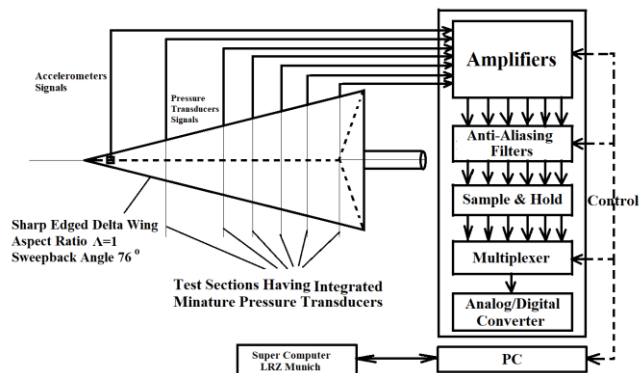


Figure 9: Data acquisition System

III. RESULTS AND DISCUSSIONS

3.1. Numerical calculations of the wing structure deformation

Numerical calculations have been utilized to predict the structure deformation of the wing under the aerodynamic loads at different angles of attack and free stream speeds. The elastic deformation of the delta wing especially at the apex has an important influence on the flow field and the vortex structure after Coe, Jr. P. L.; Weston R. P. (1979) [15]. A stiff light weight carbon fiber delta wing test model has been developed to minimize the elastic deflection of the wing by using a stiff structure and the inertia forces by using a light-weight structure. The structure deformations of the model have been calculated using the finite element program NASTRAN with the pre and post processing program PATRAN. The predicted steady-pressure data at 20° angle of attack for 24m/s and 48 m/s free stream velocity were used as input data. The generated grid structure of the wing is graphically illustrated in figures 10-11. The structure deformations in Z-direction, normal to the leeward surface of the model at an angle of attack of 20° and free stream velocity of 48m/s , is represented graphically in figures 12 and 13 with a maximum deflection close to the apex of 0.464 mm or 0.00069 in dimensionless form by dividing the deformation by the wing chord “Cr”. By increasing the free stream velocity to 48m/s at the same angle of attack of 20° , the maximum

deflection close to the apex increases to about 0.487 mm or 0.00073 in a dimensionless form, while this value was 0.496 mm or 0.0007 in a dimensionless form for free stream velocity of 48m/s and angle of attack of 32.5° . These values are far below the critical values and are of negligible effect on the vortex flow over the wing.

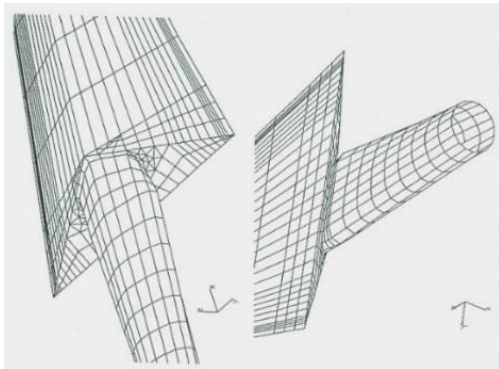


Figure10: Grid structure of the delta model

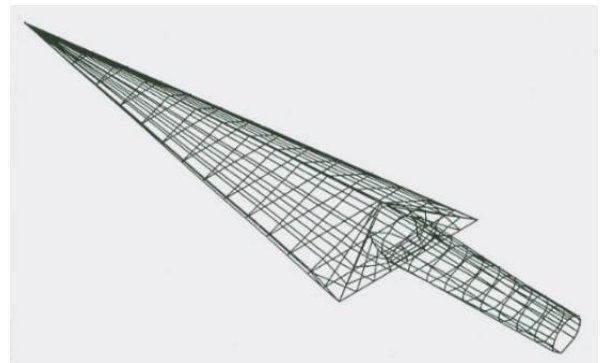


Figure 11: Grid structure of the delta model

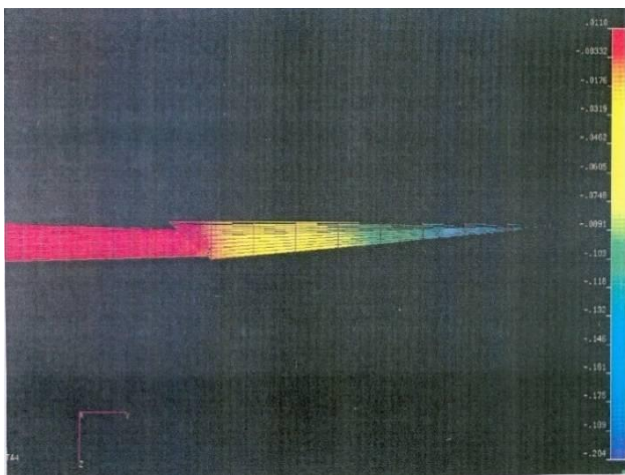


Figure12: Structure deformation in z direction

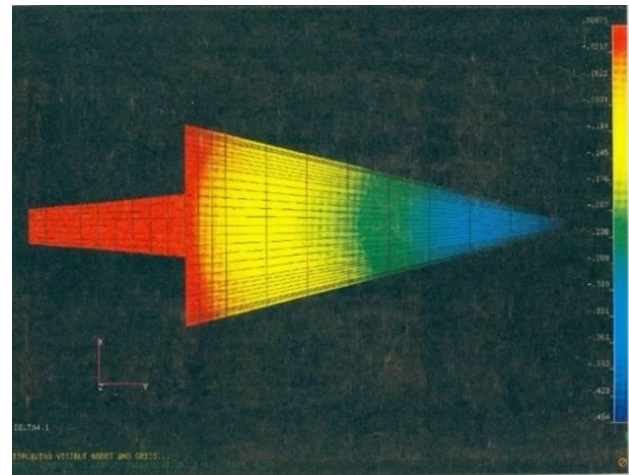


Figure13: Structure deformation in z direction

3.2. Surface suction pressure on the leeward side of the wing

For zero angle of attack, the location of the maximum surface suction pressure on the leeward side of the wing for all five test sections were located at $y/(S/2)=0.9$ with highest values of suction pressure of $-C_p = 0.12$ and 0.121 on both symmetrical sides of the wing as shown in figure 20. These values decreases by moving toward the apex up to a value of $-C_p = 0.046$ at $x/C_r=0.3$ as shown in figure 14 which is a good indication that the primary vortex in the rear part of the wing is better formed than close to the apex and confirm that the vortex starts its formation at the rear part of the

wing leading edge close to the trailing edge and moves from there upstream toward the apex. The reason for the presence of the suction pressure and their peaks at all lateral cross sections, shown in figure 20, as indication of the formation of the vortex at these locations at zero angle of attack is the chambered section configuration of the wing. It is to be noted that the values of the surface suction pressure at $x/Cr=0.5$ at the mid wing have the lowest values among all other lateral cross sections upstream as well as downstream of this section as shown in figure 14. These values are increased slightly by moving upstream to $x/Cr = 0.3$ close to the apex while increased remarkably by moving downstream toward the trailing edge as have been predicted at $x/Cr=0.7, 0.8$ and 0.9 as shown in figure 14.

By increasing the angle of attack to 2.5° , the maximum surface suction pressure coefficient “ $-C_p$ ” at all cross sections were increased in values, as indication of increased vortex strength, and moved inward away from the leading edge to $y/(S/2)=0.8$, as indication of a more developed vortex structure of bigger diameter as shown in figure 15. The test section of the maximum surface suction pressure coefficient “ $-C_p$ ” moved upstream from $x/Cr=0.9$ at zero degree angle of attack to $x/Cr=0.8$ at 2.5° angle of attack as shown in figure 15, having a values of $-C_p = 0.289$ and 0.281 at $x/Cr = 0.9$ on both symmetrical sides of the wing, as shown in figure 20, is due to the increased adverse pressure gradient aft the trailing edge due to the increased the angle of attack.

At 5° angle of attack, the maximum suction pressure moved inward from the leading edge towards the axis of symmetry at $y/(S/2) = 0.75$ for all cross sections as shown in figure 16. Its highest value is $-C_p = 0.403$ at $x/Cr = 0.9$ on both symmetrical sides of the wing as shown in figure 20, while this values becomes $-C_p = 0.539$ at $x/Cr = 0.8$ as shown in figure 16.

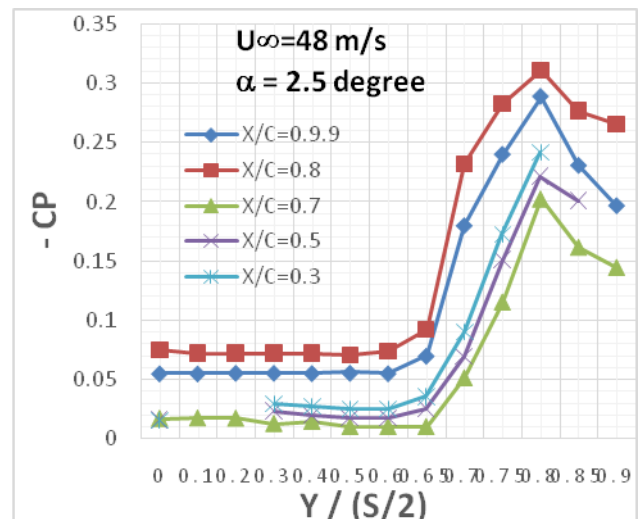
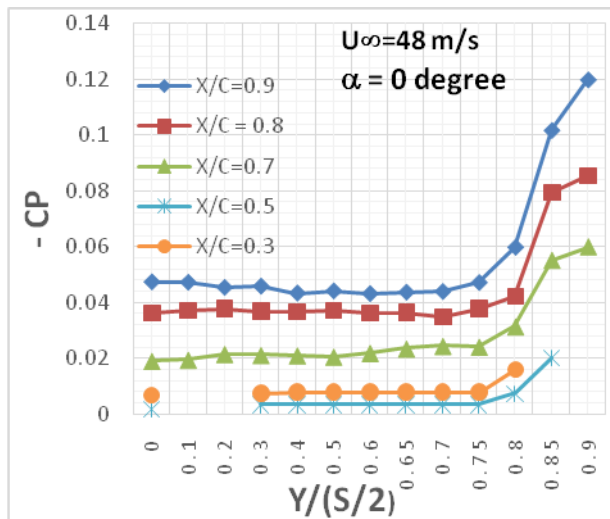


Figure 14: C_p distribution at $\alpha = 0^\circ$ Figure 15: C_p distribution at $\alpha = 2.5^\circ$

At 7.5 degree angle of attack, the maximum suction pressure is still at the cross section of $y/(S/2) = 0.75$ with the highest value of $-C_p = 0.5075$ and 0.5081 at $x/C_r = 0.9$ as shown in figure 20 and is moved from $x/C_r = 0.8$ in the rear part of the wing upstream toward the apex at $x/C_r = 0.3$ with $-C_p = 0.648$, as shown in figure 17, because the vortex strength was increased with fully developed vortex structure in the region close to the apex and far from the effect of the adverse pressure gradient downstream aft the trailing edge, which increases by increasing the angle of attack and also due to the kinking of the vortex core upward

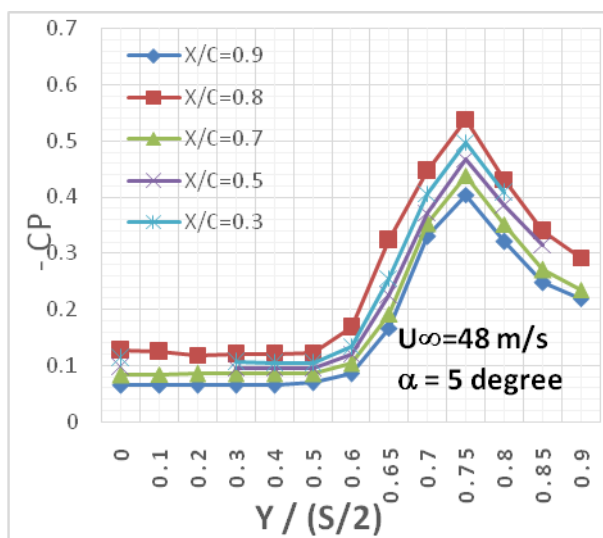


Figure 16: Cp distribution at $\alpha = 5^\circ$

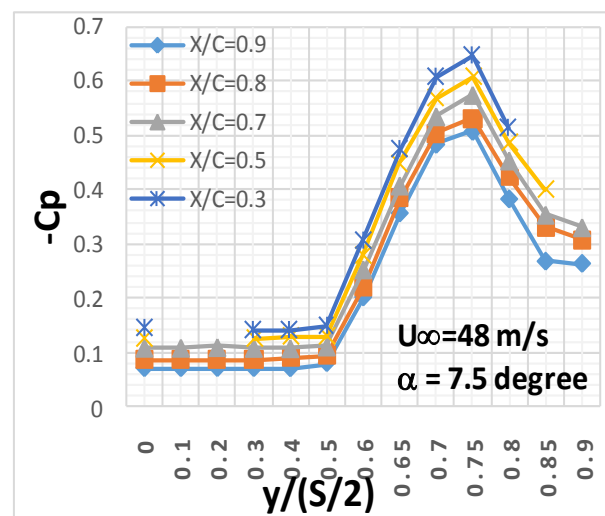


Figure 17: Cp distribution at $\alpha = 7.5^\circ$

At an angle of attack of 10° , the suction pressure on the leeward side of the wing increase to maximum values of $-C_p = 0.592$ and 0.599 at $y/(S/2) = 0.7$ and $x/C_r = 0.9$ on both symmetrical sides of the wing as shown in figure 20, up to $-C_p = 0.935$ at $x/C_r = 0.3$ as shown in figure 18.

Increasing the angle of attack to 12.5° results in increasing the suction pressure on the leeward side of the wing to maximum values of $-C_p = 0.699$ and 0.701 at $y/(S/2) = 0.7$ and $x/C_r = 0.9$ on both symmetrical sides of the wing as shown in figure 20, up to $-C_p = 0.785$ at $x/C_r = 0.3$ as shown in figure 19. A secondary vortex is indicated by the presence of second suction peaks of a value of $-C_p = 0.460$ at $y/(S/2) = 0.85$ on both symmetrical sides of the wing at $X/C_r = 0.9$ as shown in figure 20. The effect of increasing the angle of attack on the surface suction pressure on the leeward side of the wing results in increase in their values and leads to inboard movement of the maximum suction peaks as indicator of the location of the primary vortex as shown in figure 20

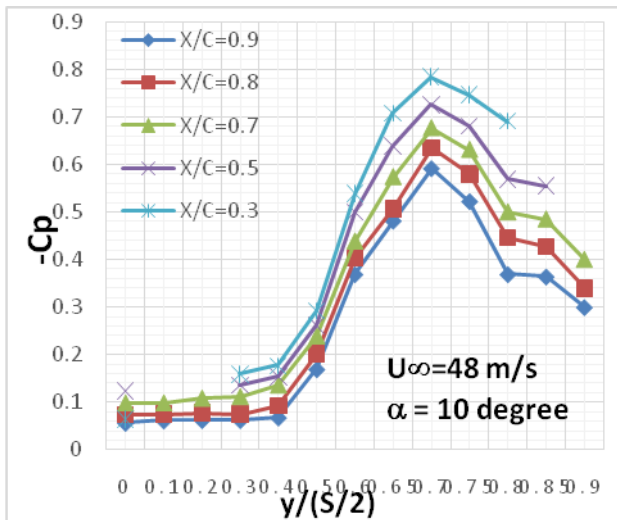


Figure 18: Cp distribution at $\alpha = 10^\circ$

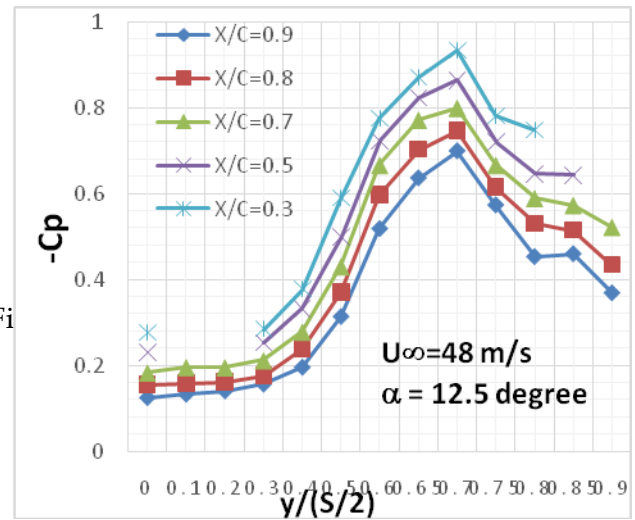


Figure 19: Cp distribution at $\alpha = 12.5^\circ$

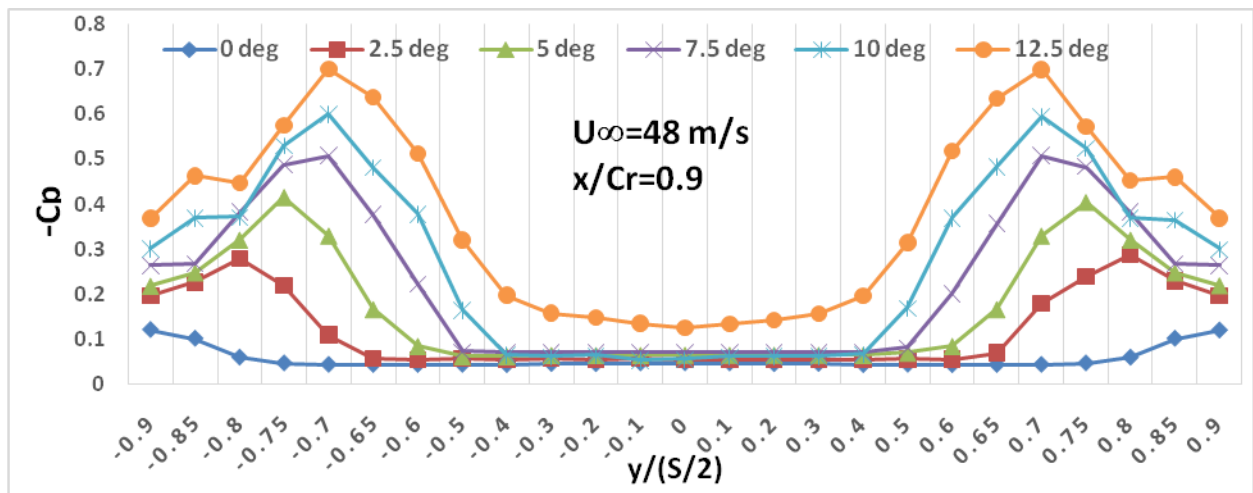


Figure 20: Cp distribution at α from 0 to 12.5° at $x/Cr=0.9$

Increasing the angle of attack to 15° leads to the inboard movement of the maximum suction pressure location on the right side of the wing to the new location at $y/(S/2) = 0.65$ while remains unchanged on the left side of the wing at $y/(S/2) = 0.7$ on the left side with corresponding values of $-C_p = 0.673$ and 0.758 respectively as shown in figure 24. Further increase in the angle of attack to 20° leads to the inward displacement of the maximum suction pressure to the new location at $x/Cr = 0.9$ and $y/(S/2)$ of 0.75 on the left side of the wing, while remains unchanged on the right side of the wing at the location of $y/(S/2) = 0.75$ having values of $-C_p = 0.881$ and 0.879 respectively as in figure 22. The second suction peaks remain unchanged in their values having the same values obtained at 12.5° angle of attack

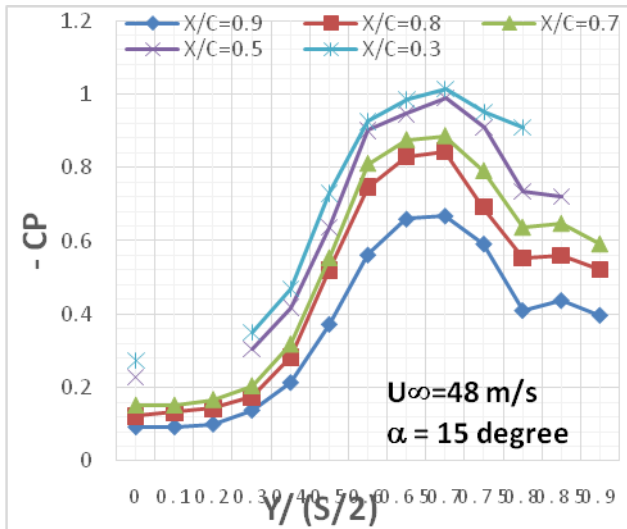


Figure 21: Cp distribution at $\alpha = 15^\circ$

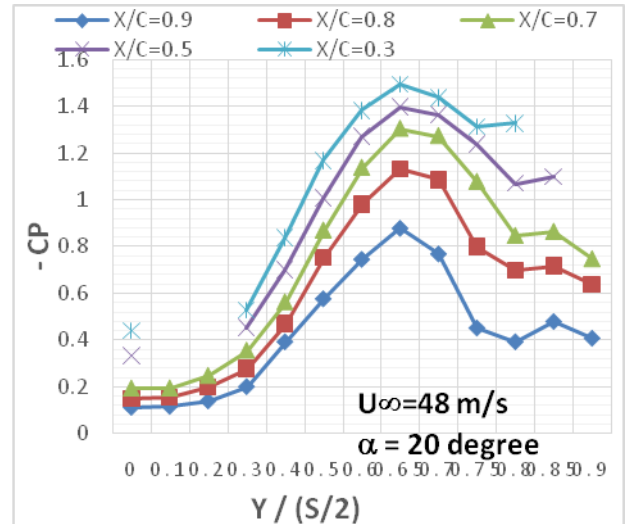


Figure 22: Cp distribution at $\alpha = 20^\circ$

At 25° angle of attack, the leading-edge vortices are stable from the apex to the trailing edge due to the increased vortex strength as it can be predicted from the surface suction pressure distribution on the leeward side of the wing in figure 23. The maximum suction pressure as indication of the primary vortex lie at $y/(S/2) = 0.996$ and 0.991 on the right and left sides of the symmetrical line of the wing respectively at $X/C_r=0.9$ as shown in figure 24 combined with second peaks of the suction pressure as indicator of the location of a secondary vortex having values of $-C_p = 0.469$ and 0.461 on the right and left symmetrical sides of the wing respectively at $y/(S/2) = 0.85$ for both sides as shown in figure 24. The development of the suction pressure on the leeward side at $X/C_r=0.9$ for the angles of attack from 12.5° to 25° are shown in figure 24.

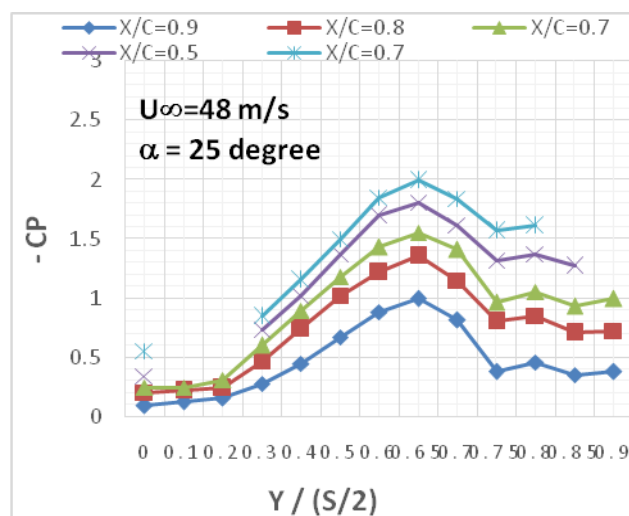


Figure 23: Cp distribution at $\alpha = 25^\circ$

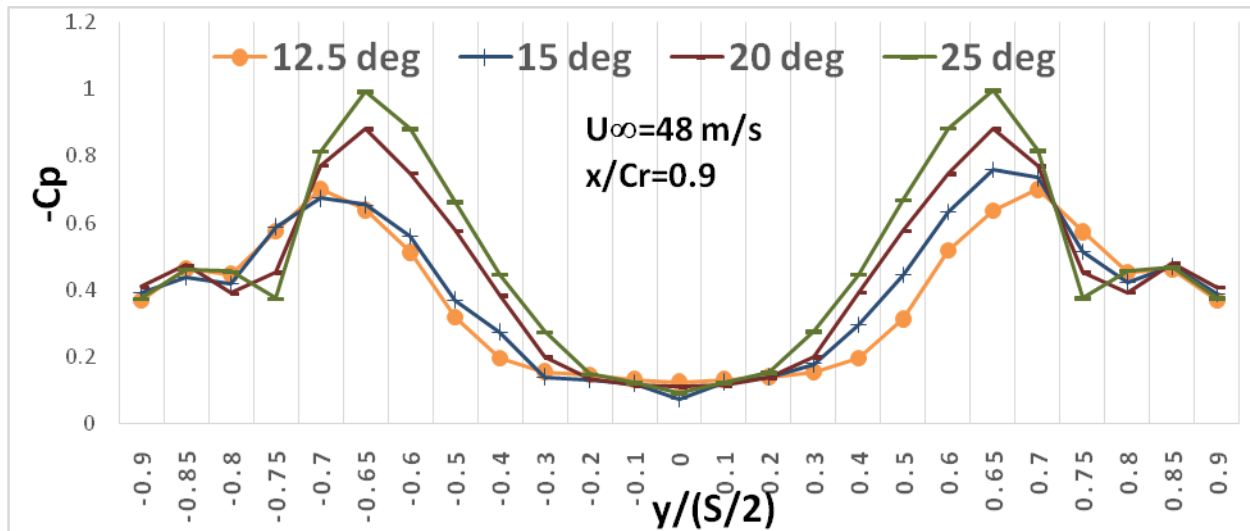


Figure24: Cp distribution at $x/Cr=0.9$ at different angles of attack.

Increasing the angle of attack to 30° results in increasing the maximum suction pressure on the leeward side of the wing at all test sections from $x/Cr = 0.3$ with a maximum value of $-C_p = 2.527$ close to the apex to $x/Cr = 0.9$ with a maximum value of $-C_p = 1.21$ close to the trailing edge in the right half of the wing as shown in figure 25. The maximum suction pressures at $x/Cr=0.9$ are $-C_p=1.206$ and 1.231 on the left and right symmetrical side of the wing respectively as shown in figure 29 with inward movement of their locations to $y/(S/2)=0.65$ on both symmetrical sides as shown in figure 29. The second suction peaks of $-C_p = 0.459$ and 0.458 were predicted on the left and right sides respectively at $y/(S/2) = 0.85$ as shown in figure 29. The primary and secondary vortices are still healthy over all test sections of the wing at this high angle of attack.

Further increase in the angle of attack to 32.5° leads to additional movement of the location of the maximum suction pressure at all test sections over the wing to a location at $y/(S/2)=0.6$ with an increase in the maximum suction pressure on the leeward side of the wing at all test sections from $x/Cr = 0.3$ with its maximum value of $-C_p = 2.831$ up to $x/Cr = 0.9$ with its maximum value of $-C_p = 1.392$ in the right half side of the wing as shown in figure 26. The second suction peak moved outboard towards the leading edge at $y/(S/2) = 0.8$ and was predicted at the test sections of $x/Cr = 0.9, 0.8$ and 0.7 only because the bigger volume of the primary vortex in this region gives enough space for flow reattachment and for the development of secondary and tertiary separations and vortices. A third suction peak is predicted at two test sections only, namely at $x/Cr = 0.8$ and 0.7 only because the adverse pressure gradient downstream to the trailing edge and the upward kinking of the core of the primary vortex hinder the formation of the tertiary vortex close to the trailing edge as shown in figure 26. The maximum suction pressure on the leeward side of the wing at $x/Cr=0.9$ increased to values of $-C_p = 1.392$ and 1.364 with further inboard movement of their locations to $y/(S/2)=0.6$ on both symmetrical sides as shown in figure 29. The second suction peaks of $-C_p = 0.648$ and 0.662 were predicted on the left and right sides respectively at $y/(S/2) = 0.8$. A third suction peak is detected at $y/(S/2) = 0.7$ for $x/Cr = 0.8$ and 0.7 with their $-C_p=1.423$ and 1.76 respectively as shown in figure 26.

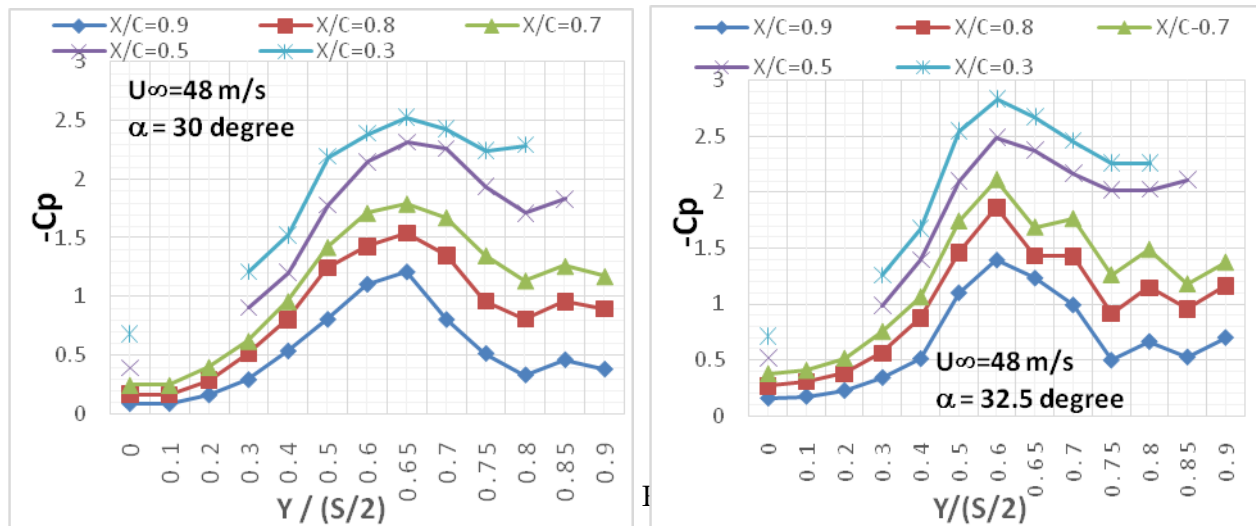


Figure 24: Cp distribution at $x/C_r=0.9$ at different angles of attack.

Increasing the angle of attack to 30° results in increasing the maximum suction pressure on the leeward side of the wing at all test sections from $x/C_r = 0.3$ with a maximum value of $-C_p = 2.527$ close to the apex to $x/C_r = 0.9$ with a maximum value of $-C_p = 1.21$ close to the trailing edge in the right half of the wing as shown in figure 25. The maximum suction pressures at $x/C_r=0.9$ are $-C_p= 1.206$ and 1.231 on the left and right symmetrical side of the wing respectively as shown in figure 29 with inward movement of their locations to $y/(S/2)=0.65$ on both symmetrical sides as shown in figure 29. The second suction peaks of $-C_p = 0.459$ and 0.458 were predicted on the left and right sides respectively at $y/(S/2) = 0.85$ as shown in figure 29. The primary and secondary vortices are still healthy over all test sections of the wing at this high angle of attack. Further increase in the angle of attack to 32.5° leads to additional movement of the location of the maximum suction pressure at all test sections over the wing to a location at $y/(S/2)=0.6$ with an increase in the maximum suction pressure on the leeward side of the wing at all test sections from $x/C_r = 0.3$ with its maximum value of $-C_p = 2.831$ up to $x/C_r = 0.9$ with its maximum value of $-C_p = 1.392$ in the right half side of the wing as shown in figure 26. The second suction peak moved outboard towards the leading edge at $y/(S/2) = 0.8$ and was predicted at the test sections of $x/C_r = 0.9, 0.8$ and 0.7 only because the bigger volume of the primary vortex in this region gives enough space for flow reattachment and for the development of secondary and tertiary separations and vortices. A third suction peak is predicted at two test sections only, namely at $x/C_r = 0.8$ and 0.7 only because the adverse pressure gradient downstream to the trailing edge and the upward kinking of the core of the primary vortex hinder the formation of the tertiary vortex close to the trailing edge as shown in figure 26. The maximum suction pressure on the leeward side of the wing at $x/C_r=0.9$ increased to values of $-C_p = 1.392$ and 1.364 with further inboard movement of their locations to $y/(S/2)=0.6$ on both symmetrical sides as shown in figure 29. The second suction peaks of $-C_p = 0.648$ and 0.662 were predicted on the left and right sides respectively at $y/(S/2) = 0.8$. A third suction peak is detected at $y/(S/2) = 0.7$ for $x/C_r = 0.8$ and 0.7 with their $-C_p=1.423$ and 1.76 respectively as shown in figure 26.

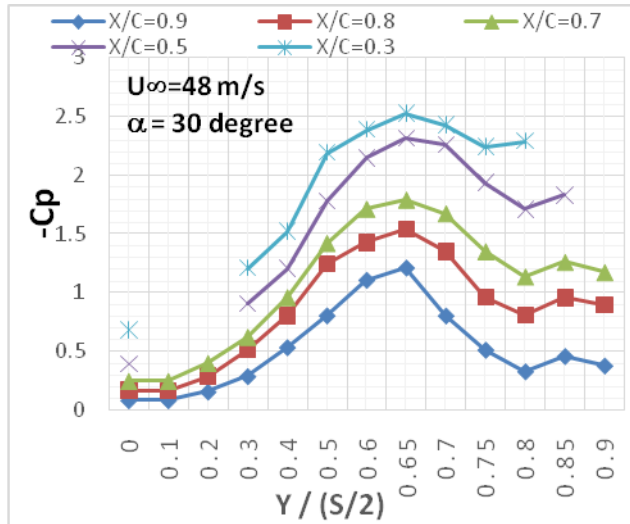


Figure 25: Cp distribution at $\alpha = 30^\circ$

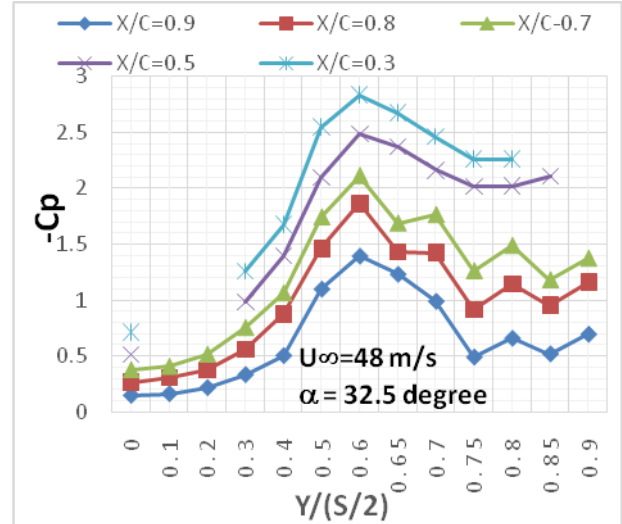


Figure 26: Cp distribution at $\alpha = 32.5^\circ$

Increasing the angle of attack to 35° results inboard movement of the location of the maximum suction pressure to $y/(S/2) = 0.6$ at all test sections and an increase in the suction pressure at $x/Cr = 0.3$ to a value of $-C_p = 2.862$, a mild decrease at $x/Cr = 0.5$ to $-C_p = 2.328$, at $x/Cr = 0.7$ to $-C_p = 1.791$, at $x/Cr = 0.8$ to $-C_p = 1.541$ and at $x/Cr = 0.9$ to $-C_p = 1.21$ as shown in figure 27. The sharp drop in the suction pressure in the rear part of the wing aft $x/Cr = 0.7$ is due to the adverse pressure gradient and the kindling of the vortex core upward from the wing and is an indication that the vortex breakdown have already reached the trailing edge and is moving upstream towards the wing apex by increasing the angle of attack. The decrease in the maximum suction pressure at $x/Cr=0.9$ is $-C_p = 1.077$ and 1.05 at $y/(S/2)=0.6$ on both symmetrical sides as shown in figure 29. The second suction peaks of $-C_p = 0.95$ and 0.902 were predicted on the right and left sides respectively at $y/(S/2) = 0.8$ and 0.85 .

At 40° angle of attack the vortex instability and, subsequently the vortex bursting location is moved further upstream toward the wing apex leading to a drastic decrease in the suction surface pressure coefficient “ $-C_p$ ” in the rear part of the wing at and aft $x/Cr=0.5$ reaching a value of $-C_p = 0.746$ and 0.753 on the right and left side of the wing respectively at $y/(S/2) = 0.65$ on both sides, while these values are barely affected upstream of the location of $x/Cr=0.5$ having values of $-C_p = 2.677$ at x/Cr of 0.3 and 2.328 at $x/Cr = 0.5$ as shown in figures 28 and 29. A comparison of these values at $x/Cr = 0.9$ for the angles of attack between 25° and 40° are presented in figure 29.

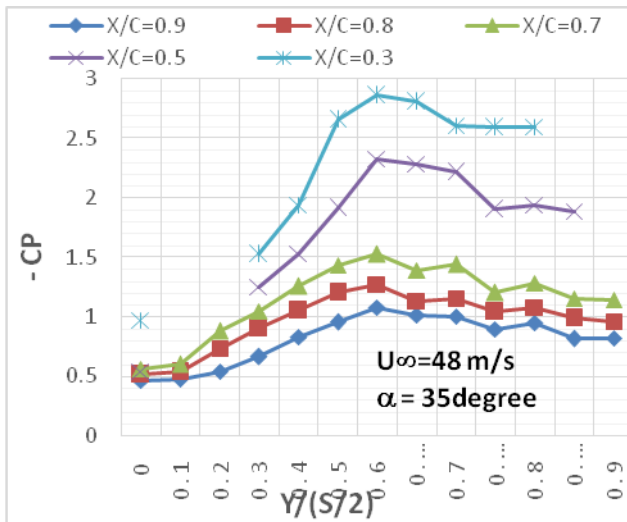


Figure 27: Cp distribution at $\alpha = 35^\circ$

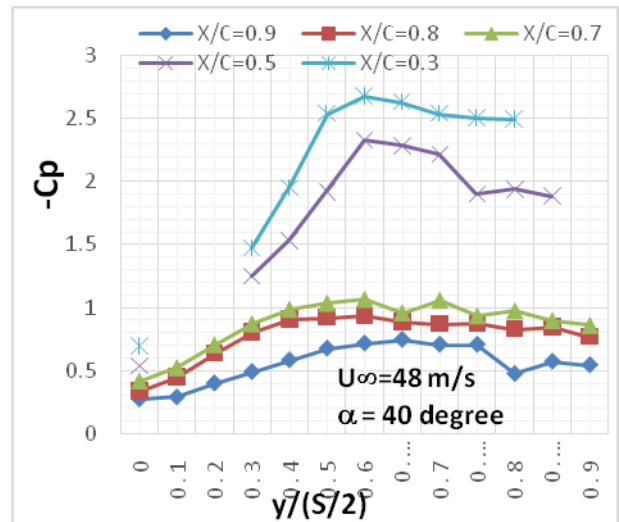


Figure 28: Cp distribution at $\alpha = 40^\circ$

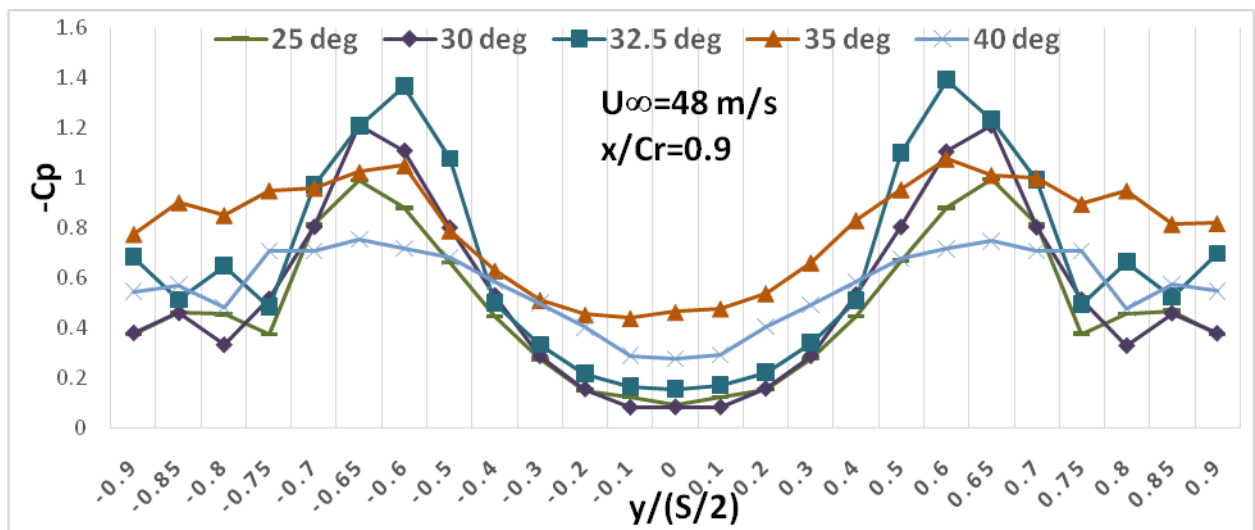


Figure 29: Cp distribution at $x/Cr=0.9$ at different angles of attack

Further increase in the angle of attack to 45° leads to apparent reduction in the surface suction pressure at $x/Cr = 0.5$ and less reduction at $x/Cr=0.3$ and more less by moving downstream toward the trailing edge reaching values of 0.723 and 0.671 for $X/Cr=0.9$ at $y/(S/2) = 0.65$ on both sides as shown in figure 30. More Increase in the angle of attack to 50° results in sharp reduction in the surface pressure coefficient “-Cp” distribution on the leeward side of the wing in the front area of the wing at $X/Cr=0.3$ having its maximum suction pressure of $-Cp=1.577$ at $y/(S/2) = 0.75$, while the first suction peaks on both side of the symmetrical line of the leeward side of the wing are $-Cp= 0.65$ and 0.576 on the right and left side respectively at $y/(S/2)= 0.65$ on both sides as shown in figure 31. For the angles of attack of 60° and 73° , the surface suction pressures of the

leeward side of the wing are located at the forward and middle part of the wing at $X/C_r=0.3$ and 0.5 dropped sharply to close level as those close to the trailing edge between $-C_p=0.6$ and 0.4 at 60° angle of attack and between 0.5 and 0.3 at 73° angle of attack as shown in figure 32 and 33.

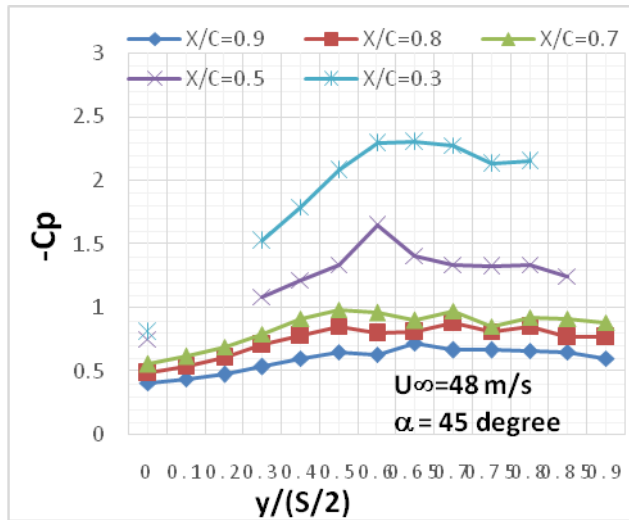


Figure 30: Cp distribution at $\alpha = 45^\circ$

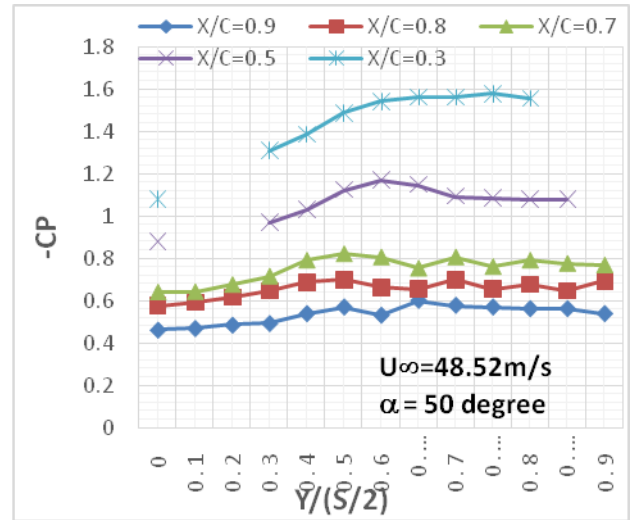


Figure 31: Cp distribution at $\alpha = 50^\circ$

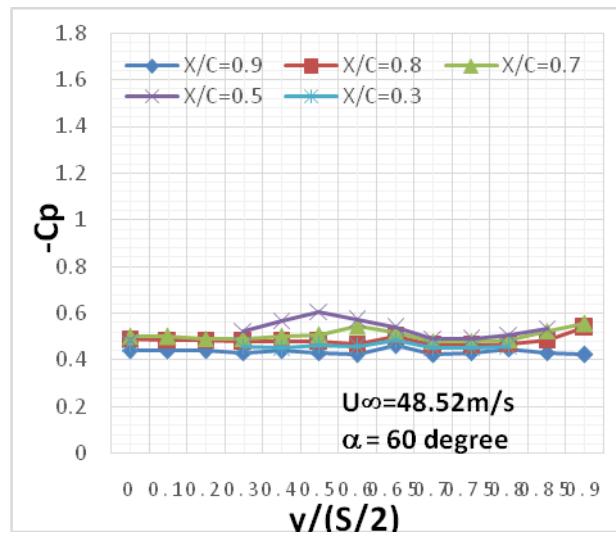


Figure 32: Cp distribution at $\alpha = 60^\circ$

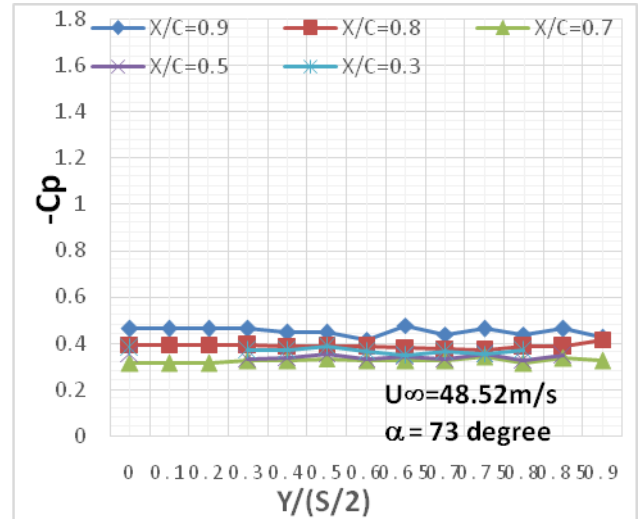


Figure 33: Cp distribution at $\alpha = 73^\circ$

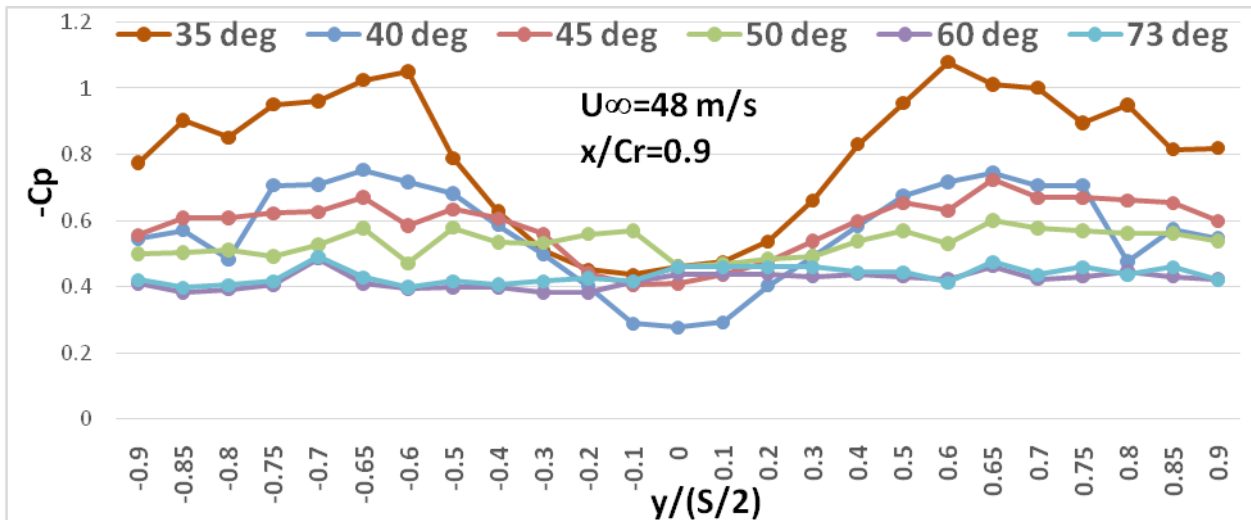


Figure34: Cp distribution at $x/Cr=0.9$ at different angles of attack

The values of the first maximum suction peak of the surface pressure coefficient “-Cp” from the line of symmetry on the leeward side of the wing at different cross sections of $x/Cr=0.3$ to 0.9 , which reflects the suction pressures underneath the core of the primary vortex, indicate mild increase in these values with small slopes by increasing the angle of attack up to 15° as shown in figure 35. Further increase of the angle of attack from 15° to 32° results in sharper linear increase in the maximum suction pressure at all cross sections with remarkably increased slopes by moving upstream toward the apex.

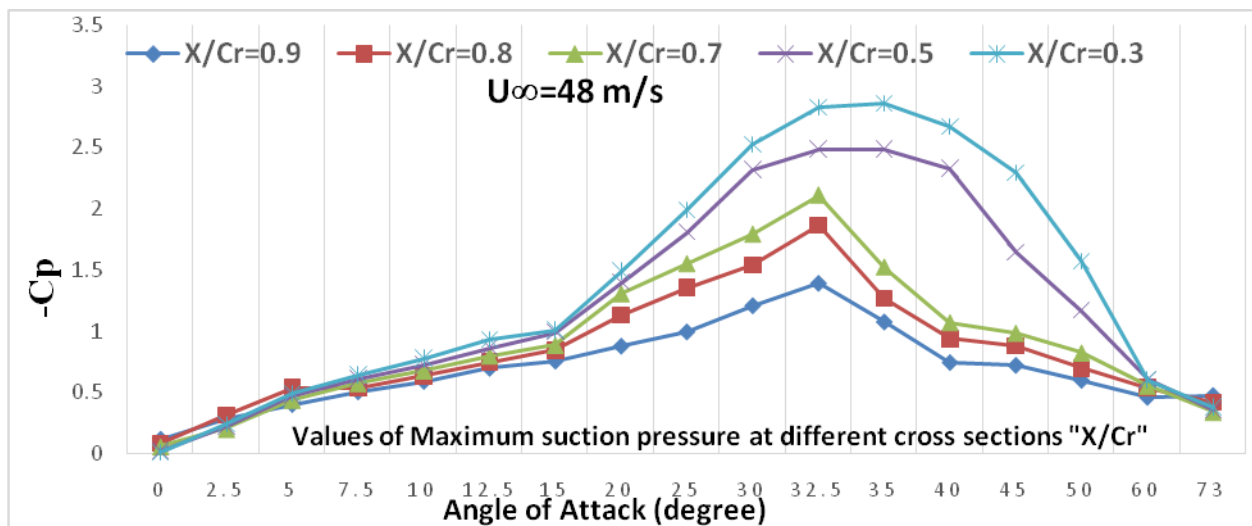


Figure 35: Maximum suction pressure at different cross sections downstream the apex

By increasing the angle of attack over 32.5° results in sharp decrease in the value of the maximum suction pressure at cross section of $x/Cr=0.9$, 0.8 and 0.7 up to an angle of attack of 32.5° followed by mild decrease for the cross the sections of $x/Cr=0.3$ and 0.5 upto 40° followed by sharp drop by increasing the angle of 40° while the maximum peaks of the surface suction pressures in the region

aft the apex downstream up to the cross section of $x/Cr=0.5$ are remarkably higher in values comparable to the rest of the wing at $x/Cr=0.7, 0.8,$ and 0.9 and are increasing in values by increasing the angle of attack up to 35° followed by mild decrease in the maximum suction pressure by further increase of the angle of attack to 40° and sharp fall in their values by additional increase to 60° approaching very a close or common value for all cross section covering the whole wing from the apex to the trailing edge followed by little decrease in their values by further increase in the angle of attack to 73° .

The trajectory of the location of the first surface suction peaks from the symmetrical line of the leeward side of the delta wing on their left and right sides as an indicator of the location of the primary-vortex core at different cross sections from $x/Cr = 0.3$ to 0.9 showing their inward movement for all cross sections toward the symmetrical line by increasing the angle of attack up to 35° followed by different trajectories depending on its distance from the apex by further increase up to 73° as illustrated in figure 36.

The trajectory of the first and second surface suction peaks on both symmetrical leeward sides of the delta wing on their left and right sides as an indicator of the location of the primary and secondary vortices are illustrated in figure 37. It indicates an inward movement of the first suction peak toward the symmetrical line by increasing the angle of attack up to 32.5° and remain at this location up to 35° angle of attack, followed by reversing its movement toward the leading edge by further increase up to 73° . The secondary suction peak, as indication of the secondary vortex, have been predicted first at an angle of attack of 12.5° and $y/(S/2) = 0.85$ on both symmetrical sides of the wing and remains at this location by increasing the angle of attack to 30° .

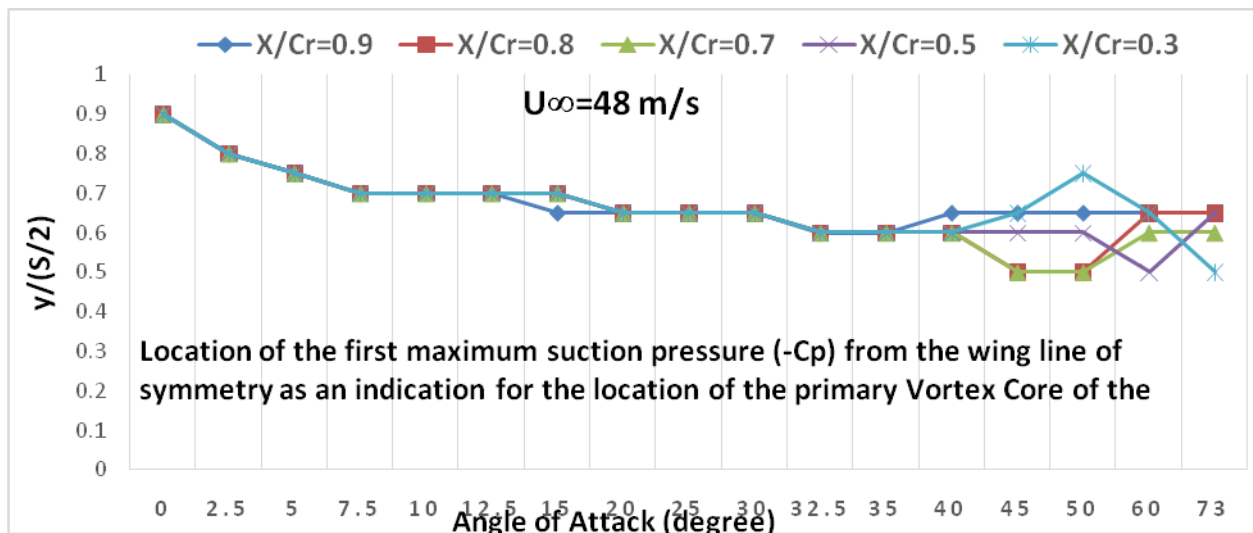


Figure 36: Trajectory of suction pressure peaks at different cross section at the apex

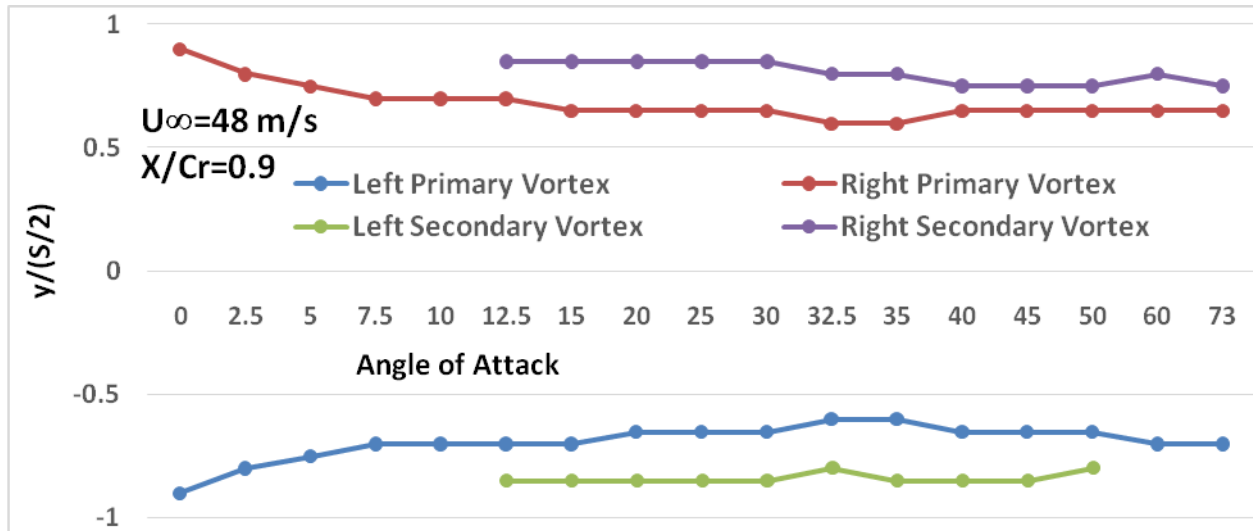


Figure37: Trajectory of the suction peaks at $x/Cr=0.9$

At 32.5° angle of attack, this location moves to 0.8 on both symmetrical sides of the wing while at 35° they remains at this location on one symmetrical side of the wing while it moves to $y/(S/2)=0.85$ on the other symmetrical side of the wing and remains at this location up to an angle of attack of 45° followed by inboard movement to $y/(S/2)=0.8$ at an angle of attack of 50° and is not predictable on this symmetrical side of the wing at angles of attack over 50° , while on the other symmetrical side of the wing it remains at $y/(S/2)=0.75$ for the angle of attack from 40° to 50° moved outboard to $y/(S/2)=0.8$ at 60° angle of attack followed by inboard movement to $y/(S/2)=0.75$ at 73° angle of attack.

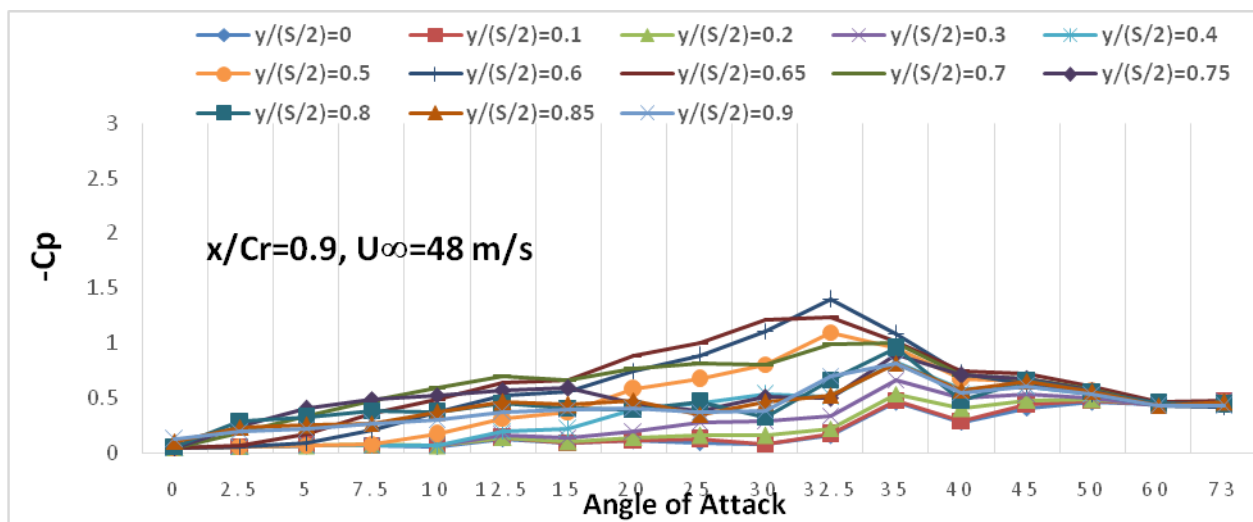


Figure38: C_p distribution over the leeward side of the wing at $x/Cr=0.9$

The predicted values indicate the increase of their values for all points up to 35° for the points located at $y/(S/2) = 0.6$ up to 0.9 . These values increase up to an angle of attack of 32.5° for all points from $y/(S/2) = 0.9$ to 0.5 having their maximum value at $y/(S/2) = 0.6$ and increasing up to an angle of attack of 40° for the points of $y/(S/2) = 0.4$ and 0.3 and to 50° angle of attack for the points of $y/(S/2) = 0, 0.1$ at 50° angle of attack as shown in figure 41 and 42.

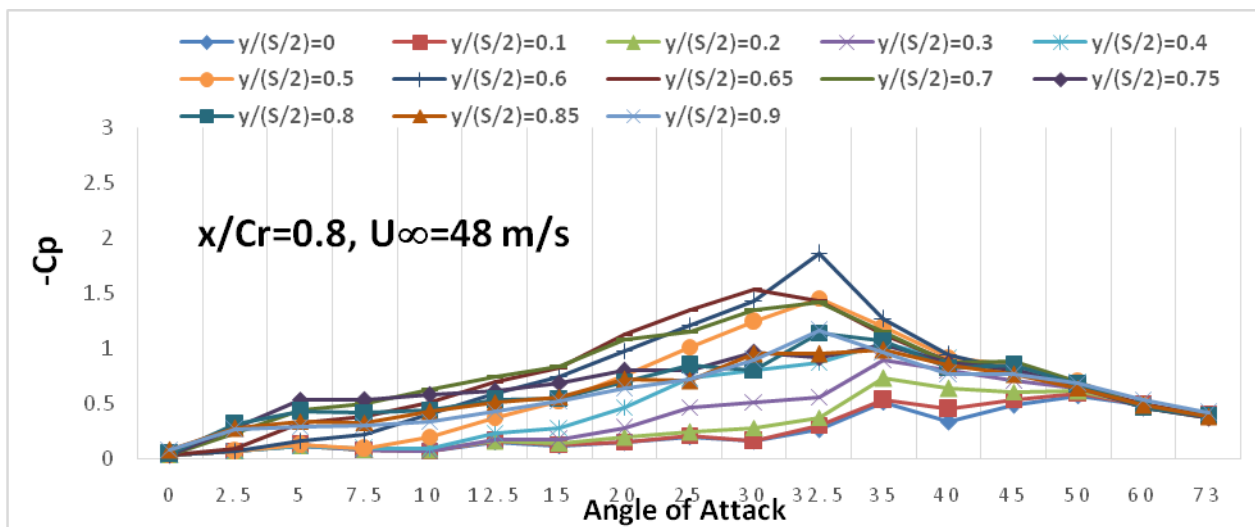


Figure 39: Cp distribution over the leeward side of the wing at $x/Cr=0.8$

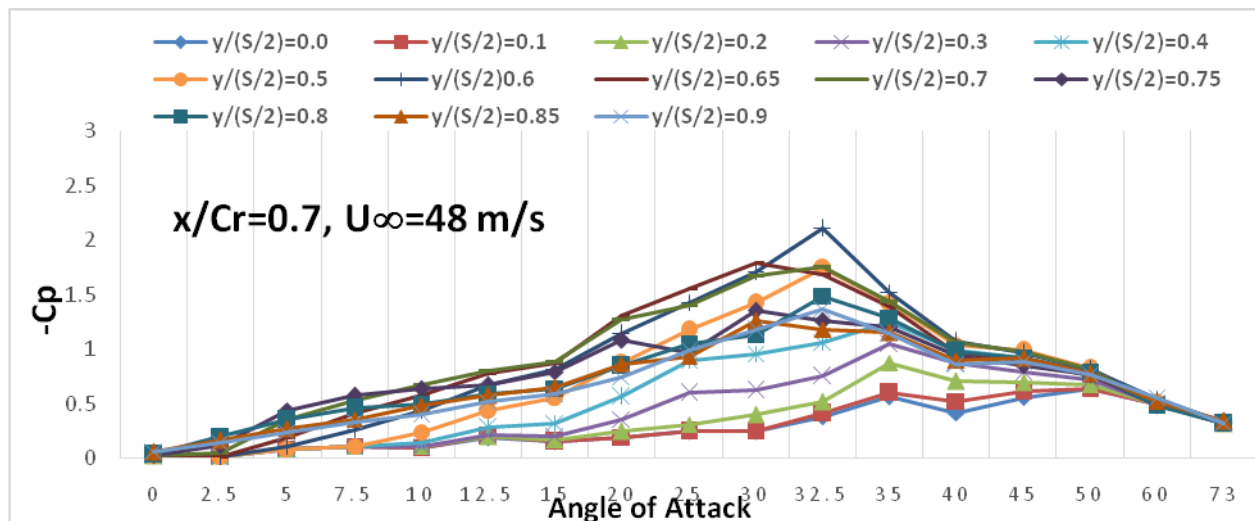


Figure 40: Cp distribution over the leeward side of the wing at $x/Cr=0.7$

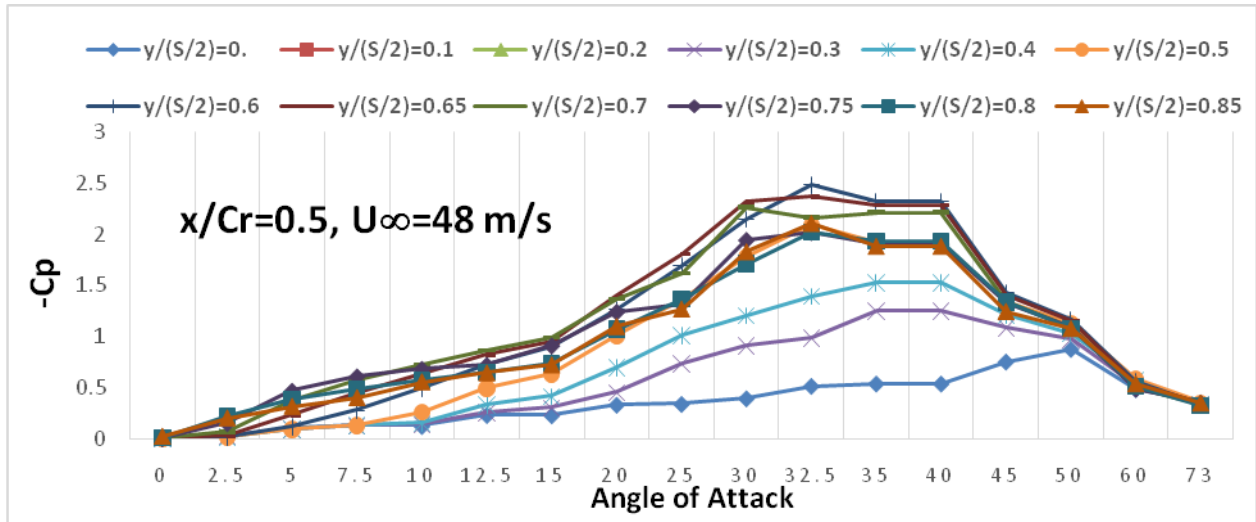


Figure41: Cp distribution over the leeward side of the wing at $x/Cr=0.5$

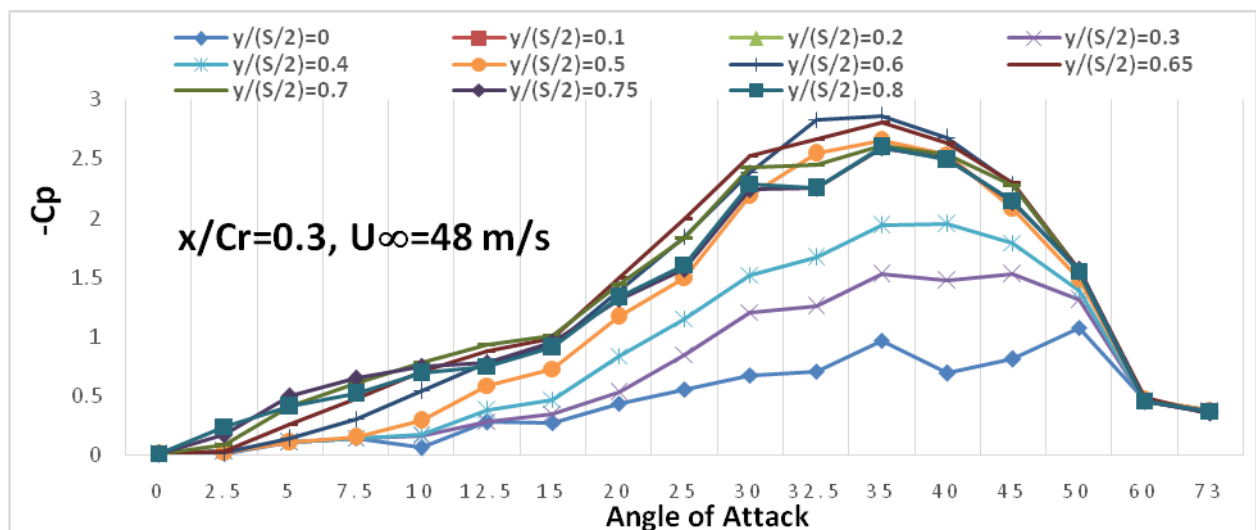


Figure42: Cp distribution over the leeward side of the wing at $x/Cr=0.3$

The predicted surface suction pressure along the cross section at $x/Cr=0.9$ at two different speeds of 24m/s and 48m/s and 10°angle of attack reflects a small Reynolds effect at $y/(S/2) = 0.85$ on both symmetrical sides of the wing, while no remarkable Reynolds effect was predicted at 32.5° angle of attack as shown in figure 43.

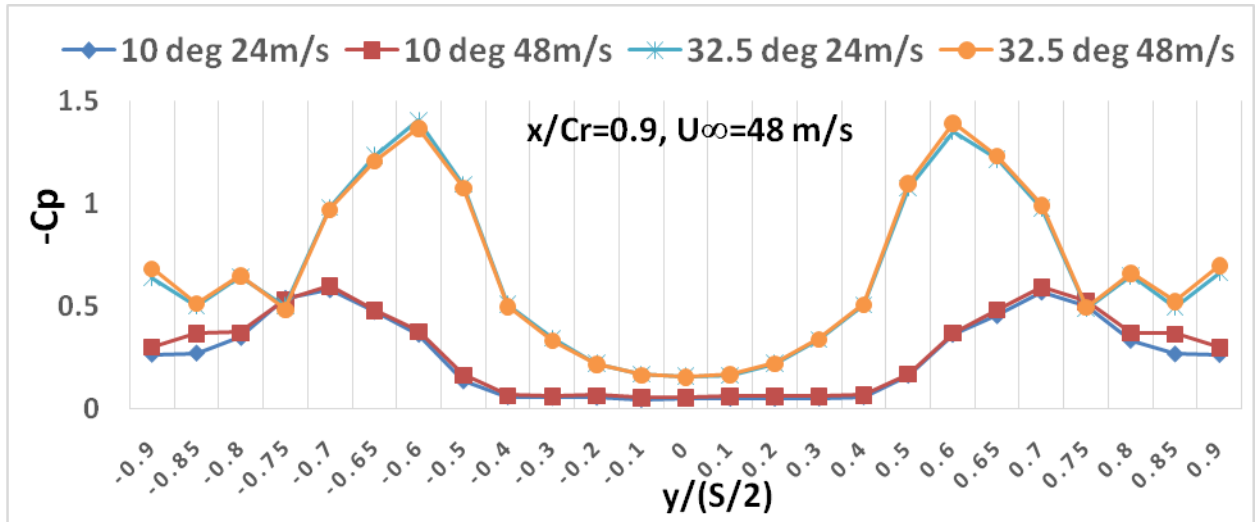


Figure 43: Cp distribution over the leeward side of the wing at $x/Cr=0.9$

Increasing the angle of attack from 32.5° , at which the maximum suction pressure peaks are predicted, to 40° reduces the suction pressure peaks of the primary vortex, and increases the suction pressure peaks of the secondary vortex on both symmetrical sides of the wing as in figure 44. The Reynolds number effect at 32.5° angle of attack is very small and increases by increasing the angle of attack up to 73° in the region between $y/(S/2)=0.7$ to 0.9 on both symmetrical sides of the wing as shown if figures 44-47.

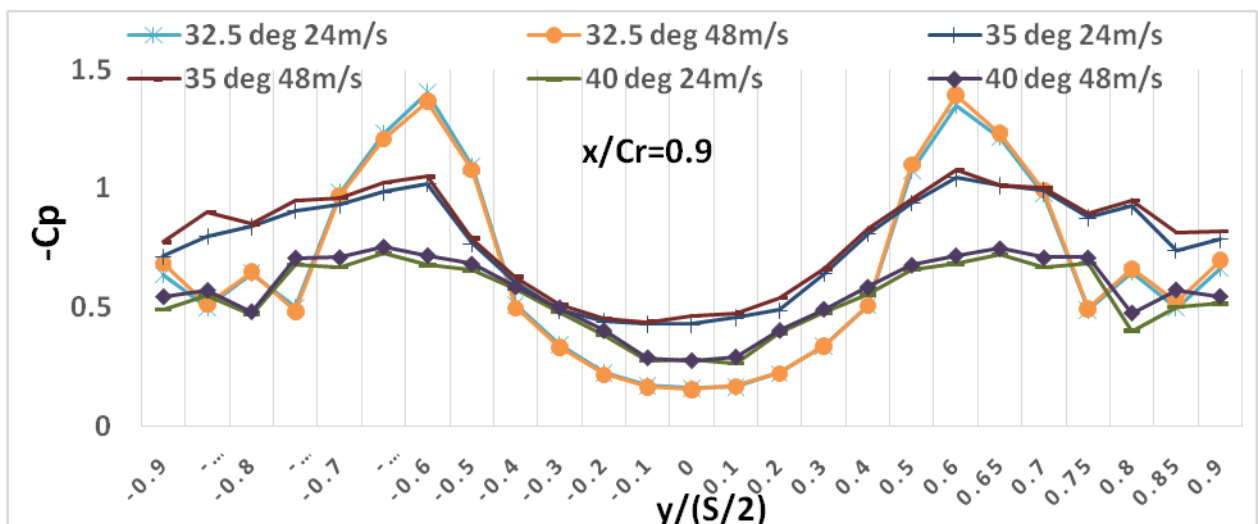


Figure 44: Cp distribution over the leeward side of the wing at $X/Cr=0.9$

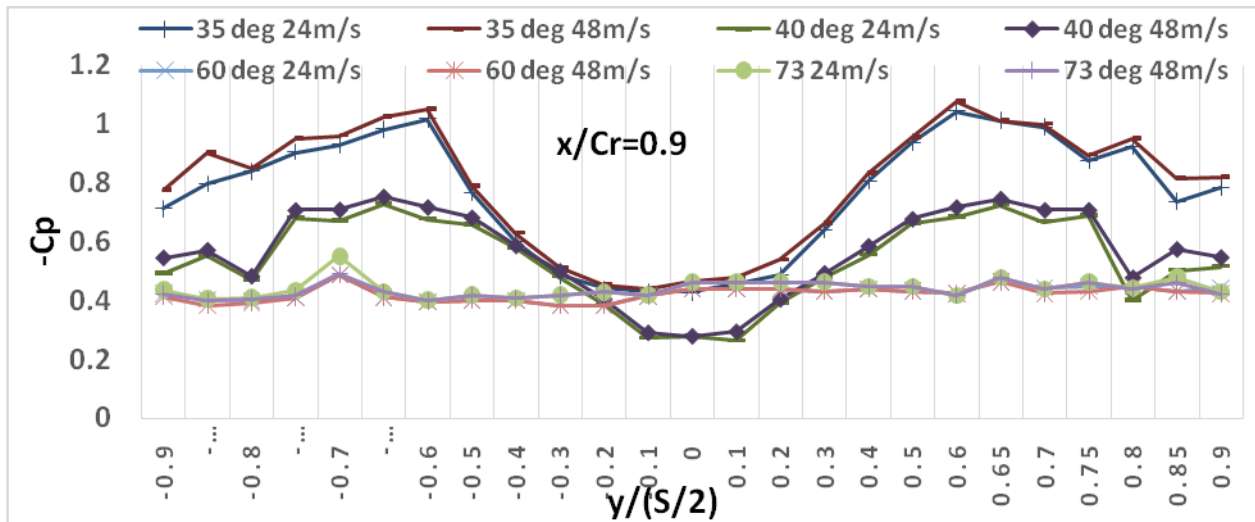


Figure 45: Cp distribution over the leeward side of the wing at $x/Cr=0.9$

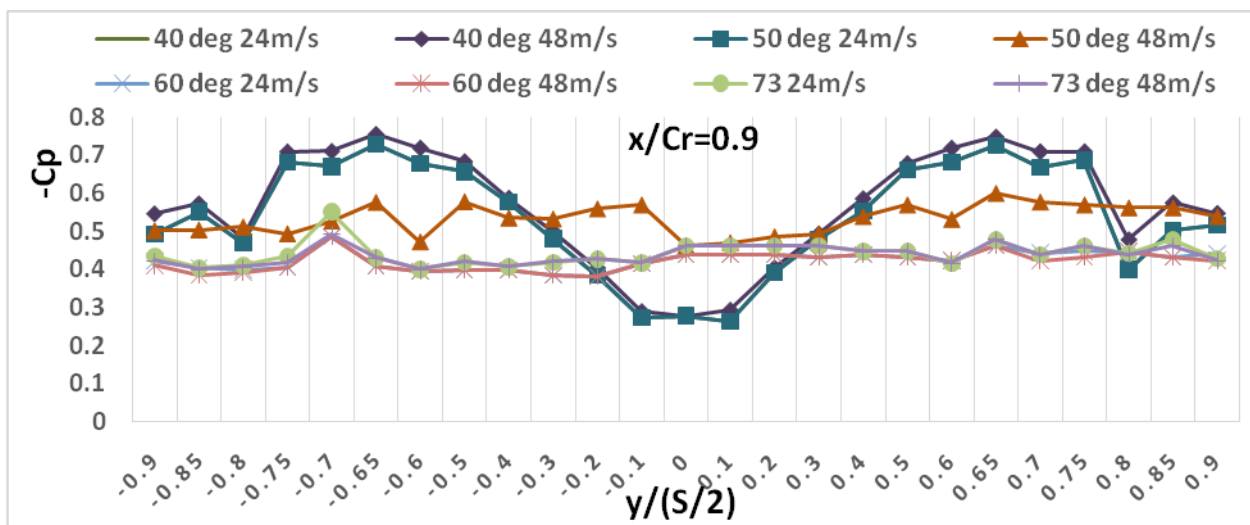


Figure 46: Cp distribution over the leeward side of the wing at $X/Cr=0.9$

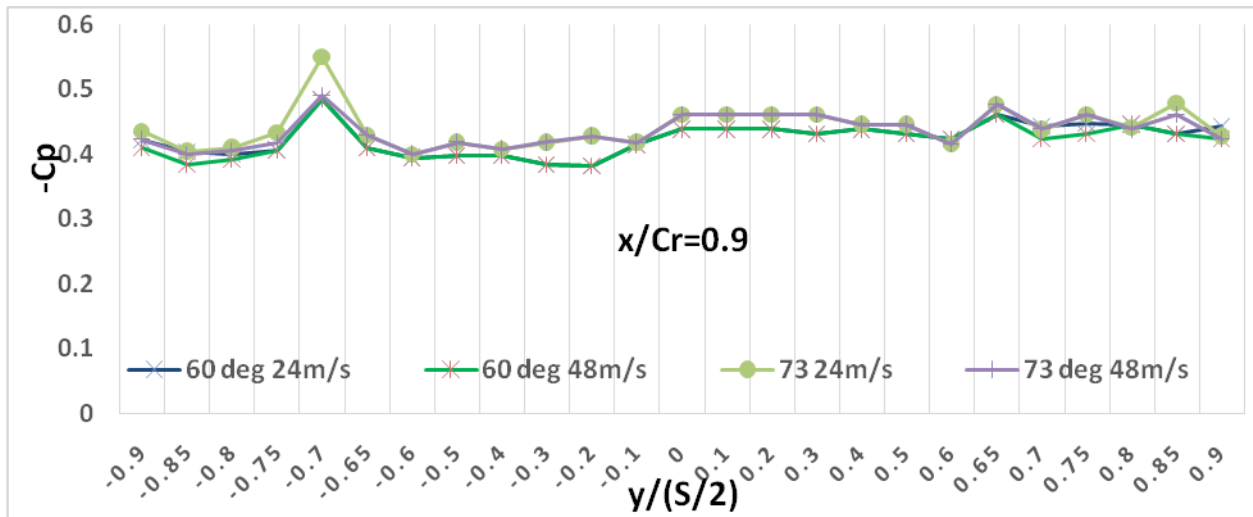


Figure 47: C_p distribution over the leeward side of the wing at $x/C_r=0.9$

IV. CONCLUSION

- In this investigation, steady surface pressure coefficient measurements were utilized on the leeside of a stiff light weight sharp edged delta wing of aspect ratio $\Lambda = 1$ and 76° sweep back angle. A stiff light weight carbon fiber delta wing test model has been developed to minimize the elastic deflection of the wing “stiff structure” and the inertia forces “light weight structure”. The measurements were acquired in a low speed wing tunnel at two different free stream speeds of 24m/s and 48m/s and for angles of attack from zero to 73° .
- Numerical calculations have been utilized to predict the structure deformation of the wing under the aerodynamic loads at different angles of attack and free stream speeds. The elastic deformation of the delta wing especially at the apex has an important influence on the flow field and the vortex structure. The structure deformations of the model have been calculated using the finite element program NASTRAN with the pre and post processing program PATRAN. The steady pressure data on the leeward and pressure sides of the delta wing acquired from the wind tunnel experiments at 20° angle of attack for 24m/s and 48 m/s free stream velocities were used as input data. The structure deformations in Z-direction, normal to the leeward side of the test model at an angle of attack of 20° and free stream velocity of 48m/s, is represented graphically showing a maximum deflection of 0.464 mm or 0.00069 in dimensionless form close to the apex. By increasing the free stream velocity to 48m/s at the same angle of attack of 20° , the maximum deflection close to the apex increases to about 0.487 mm or 0.00073 in a dimensionless form, while this value was 0.496 mm or 0.0007 in a dimensionless form for free stream velocity of 48m/s and angle of attack of 32.5° . These values are far below the critical values and are of negligible effect on the vortex flow over the wing.
- The steady surface pressure coefficient on the leeside of the delta wing have been acquired at different lateral cross sections at $x/C_r=0.3, 0.5, 0.7, 0.8,$ and 0.9 in the wind tunnel at two different speeds of 24m/s and 48m/s. At zero angle of attack the acquired pressure

coefficient values at all cross sections have shown clearly the presence of the primary vortex along the whole leading edge due to the chambered wing configuration. The values of the surface suction pressure coefficient at $x/Cr=0.5$ have the lowest values among all other lateral cross sections upstream as well as downstream of this section. These values are increased slightly by moving upstream to $x/Cr=0.3$ close to the apex while increased remarkably by moving downstream toward the trailing edge.

- Increasing the angle of attack to 2.5° , 5.0° and 7.5° resulted in increased maximum suction pressure coefficients and to the inboard movement of their locations at all cross sections from $x/Cr=0.3$ close to the apex up to $x/Cr=0.9$ close to the trailing edge as an indication of the increased primary vortex strength and diameter. The lateral cross section of the maximum surface pressure coefficient on the whole wing moves from $x/Cr=0.9$, for zero angle of attack to $x/Cr=0.8$ for 2.5° and 5.0° angles of attack, and to $x/Cr=0.3$ at 7.5° angle of attack, as a result of the increased adverse pressure gradient aft the trailing edge by increasing the angle of attack due to the kink of the primary vortex core toward the direction of the free stream velocity, any further increase in the angle of attack over 7.5° does not affect the location of the section, at which the maximum surface suction pressure exist. The surface suction pressure coefficients at the cross section of $x/Cr=0.9$ are increased by increasing the angle of attack up to an angle of attack of 35° , at which the maximum suction pressure starts its first fall because the outer shells of the primary vortices on both sides comes in contact and moves unsymmetrical upward away from the suction side of the wing by additional increase of the angle of attack. The upward movement of the primary vortex away from the leeward side of the wing reduces its effect on the surface suction pressure, which is the characteristic of the high sweep back delta wing, more than the effects of the kink of the primary vortex core and of the adverse pressure gradient downstream to this section when the vortex breakdown location approaches this section.
- The trajectory of the location of the maximum surface suction pressures at all lateral cross sections of the wing as indication of the location of the cores of the primary and secondary vortices on the wing at these sections for all angles of attack up to 73° indicated that the vortex core of the primary vortex moves inboard toward the line of symmetry of the wing with increasing the angle of attack up to 32.5° and remains fixed at this location by further increase up to 35° but on the other hand, the predicted suction pressure underneath the core axis of the primary vortex decreases remarkably by reaching the angle of attack to 35° as mentioned before. Further increase of the angle of attack over 35° results in continuous decrease in the suction pressures and their peaks at all cross sections from the apex to the trailing edges. The fall of the surface suction pressure of more cross sections closer to the apex by increasing the angle of attack over 35° reflects the upstream movement of the location of the vortex breakdown location over the wing.
- The trajectory of the location of the first surface suction peaks from the symmetrical line of the leeward side of the delta wing as indicator of the location of the primary vortex core at different cross sections from $x/Cr=0.3$ to 0.9 indicate their inward movement at all cross sections toward the symmetrical line by increasing the angle of attack up to 35° followed by different trajectories depending on their distances from the apex by further increase up to 73° as illustrated
- The predicted surface suction pressure along the cross section at $x/Cr=0.9$ at two different speeds of 24m/s and 48m/s and 10° angle of attack reflects a small Reynold effect at

$y/(S/2) = 0.85$ on both symmetrical sides of the wing, while no remarkable Reynolds effect was predicted at higher angles of attack up to 32.5° .

- Increasing the angle of attack from 32.5° to 40° reduces the suction pressure peaks of the primary vortex, and increases the suction pressure peaks of the secondary vortex on both symmetrical sides of the wing. The Reynolds number effect at 32.5° angle of attack is very small and increases by increasing the angle of attack up to 73° in the region between $y/(S/2) = 0.7$ to 0.9 on both symmetrical sides of the wing.
- The secondary suction peak, as indication of the secondary vortex, have been predicted first at an angle of attack of 12.5° and $y/(S/2) = 0.85$ on both symmetrical sides of the wing and remains at this location by increasing the angle of attack to 30° . At 32.5° angle of attack, this location moves to 0.8 on both symmetrical sides of the wing while at 35° they remains at this location on one symmetrical side of the wing while it moves to $y/(S/2) = 0.85$ on the other symmetrical side of the wing and remains at this location up to an angle of attack of 45° followed by inboard movement to $y/(S/2) = 0.8$ at an angle of attack of 50° and is not predictable on this symmetrical side of the wing at angles of attack over 50° , while on the other symmetrical side of the wing it remains at $y/(S/2) = 0.75$ for the angle of attack from 40° to 50° moved outboard to $y/(S/2) = 0.8$ at 60° angle of attack followed by inboard movement to $y/(S/2) = 0.75$ at 73° angle of attack.

REFERENCES

1. Thorpe, S. A. 1968 A method of producing a shear-flow in a stratified fluid. J. Fluid Mech. 32, 693-704.
2. Thorpe, S. A. (1971). Journal of Fluid Mechanics 46: 299-319 (1971).
3. Richardson Lewis Fry (1922). Weather Prediction by Numerical Process, Second Edition, Cambridge University Press, ISBN: 0-521-68044-1 (250pp)
4. Taylor, G. I., (1931). Effect of variation in density on the stability of superposed streams of fluid. Proc. R. Soc. London A, 132, 499-523.
5. Piercy N.A.V. (1923). On the vortex pair quickly formed by some aerofoils, J. R. Aeronaut. Soc. 27 488-500.
6. Winant, C. D.; Browand, F. K. (1974). Vortex Pairing: The Mechanism of Turbulent Mixing-Layer Growth at Moderate Reynolds Number, in: Journal of Fluid Mechanics, pp 237-255, Vol. 63, Part 2, 1974.
7. Omar Salaheldin H., Adam Saad A. (2020) Wind Tunnel Flow Visualization over a Delta Wing, Volume 6, Issue 7, 2020.
8. Earnshaw, P. B (1962). An experimental investigation of the structure of a leading edge vortex. ARC R & M 3281, 1962.
9. Sarpkaya, T. (1971). Vortex Breakdown in Swirling Conical Flows, in: AIAA Journal, pp 1792-1799, Vol. 9, No. 9, April 1971.
10. Leibovich S. (1979). The structure of vortex breakdown, Annual Review Fluid Mech. 10, 221 (1978).
11. Garg, A.K.; Leibovich, S. (1979). Spectral Characteristics of Vortex Breakdown Flowfields,

- Physics of Fluids, Vol. 22, No. 11, 1979, pp. 2053-2064. Unsteady Aspects of Leading-edge Vortices RTO-TR-AVT-080 6 -33
12. Schade, H.; Michalke, A. (1962) Zur Entstehung von Wirbeln in einer freien Grenzschicht, in: Zeitschrift für Flugwissenschaften, Heft 4/5, pp 147-154, Oktober 1962.
 13. Hall, M.G. (1972). Vortex breakdown. Ann. Rev. Fluid Mech. 4, 195-218 (1972)
 14. Coe, Jr. P. L.; Weston R. P. (1979). Effects of Wing Leading-Edge Deflection on Low-Speed Aerodynamic Characteristics of a Low-Aspect-Ratio Highly Swept Arrow-Wing Configuration, in: NASA Technical Paper 1434, June 1979.